Low frequency modes on two fringing reefs: Observations & dynamics

A THESIS SUBMITTED TO
THE GLOBAL ENVIRONMENTAL SCIENCE
UNDERGRADUATE DIVISION IN PARTIAL FULFILLMENT
OF THE REQUIREMENTS FOR THE DEGREE OF

Bachelor of Science

IN

Global Environmental Science

May 2013

By:

Hyang Yoon

Thesis Advisor:

Janet M. Becker

I certify that I have read this thesis and that, in my opinion, it is satisfactory in scope and quality as a thesis for the degree of Bachelor of Science in Global Environmental Science.

Thesis Advisor

Janet M. Becker
Department of Geology & Geophysics

Dedicated to my grandfather

Dr. Jong Teck Kim

October 1929 – December 2010

ACKNOWLEDGMENTS

First and foremost, I would like to express my sincere gratitude to my thesis advisor Janet Becker for her continuous support, patience, motivation, enthusiasm and extensive knowledge. Her guidance helped me throughout my research and while writing this thesis. I could not have imagined having a better advisor and mentor for my studies. Besides my advisor, I would also like to thank all the other professors and staff in the School of Ocean and Earth Science and Technology. Especially Mark Merrifield for helping me create the codes that were vital to my research, for his encouragement and for his generous support.

I would also like to thank NSF who funded the research and to the group that set up and collected the data for this study. If not for these supporters, this research would not have been possible. My sincere thanks goes to Ricky Fong's family for supporting my study through the Ricky Chi Kan Fong Memorial Scholarship. Being an international student is not easy and their support helped me achieve where I am today.

I send my thanks to my fellow GES members for the stimulating discussions, for the stress we shared and for all the fun we have had together. I thank my friends, spread all over the world, for their continuous support. I also thank my second family in Hawai‘i, the people of the Ohnishi residence. Thank you for supporting me from the first day I arrived on this island and for providing me a home, miles away from Japan.

Last but not the least, I would like to thank my own family. Especially my parents, TaeHo Yoon and HyangJa Kim, for supporting me unconditionally throughout my life, and my older brother Seob Yoon for introducing me to Hawai‘i and, thus, making it possible for me to study at the University of Hawai‘i at Mānoa.

ABSTRACT

Surface gravity waves are an important physical feature of the ocean that affect nearshore processes, such as coastal inundation. Wave driven inundation results from increased coastal water levels due to high and low frequency waves, breaking wave set-up and the tide. To understand and predict wave driven inundation over a fringing reef, it is necessary to relate incident wave conditions to the response at the coast. In this study, we focus on observations and dynamics of the high and low frequency waves. Bottom pressure measurements across two fringing coral reefs in the Republic of the Marshall Islands are analyzed in an effort to relate incident wave energy measured on the fore reef to the energy at the shoreline. Time series of significant wave height in the high and low frequency bands are examined, and the records with large wave energy are identified and analyzed spectrally. The largest observed shoreline response is due to low frequency motions on the reef flat. Spectral peaks during the largest events occurred at a period $T_0 = 4L/\sqrt{gh}$ which is consistent with the excitation of a quarter wave length normal mode on the reef flat. The amplitude of this normal mode increases shoreward leading to enhanced low frequency energy at the shoreline.

TABLE OF CONTENTS

LIST OF TABLES

Table **Page**

LIST OF FIGURES

Figure **Page**

LIST OF ABBREVIATIONS AND SYMBOLS

a	Amplitude
CMI	Short for College of the Marshall Islands at Majuro Atoll
CMI 2	Sensor 2 on the reef flat at CMI
CMI 4	Sensor 4 on the reef flat at CMI
CMI 7	Sensor 7 one the fore reef at CMI
$\boldsymbol{\eta}$	Free surface elevation
f	Frequency (inverse of the period, $1/T$)
$\mathbf{f}_n$	Modal frequency, where n are non-negative integers (inverse of the modal period, $1/T_n$)
g	Gravitation acceleration (9.81 m/s^2)
h	Water depth/water level
H	Wave height
Hz	Hertz
IG	Infragravity (low frequency)
k	Wave number
$\mathbf{K}_p$	Pressure response factor
L	Cross shore length of the reef flat
$\boldsymbol{\lambda}$	Wavelength
m	Meters
min	Minutes
$\boldsymbol{\omega}$	Angular frequency ($2\pi f$)
P	Bottom pressure
$\boldsymbol{\rho}$	Density of water
ROI	Short for Roi-Namur at Kwajalein Atoll
ROI 1	Sensor 1 on the reef flat at ROI
ROI 3	Sensor 3 on the reef flat at ROI
ROI 5	Sensor 5 on the fore reef at ROI
sec (or s)	Seconds
SS	Sea and swell (high frequency)
T	Period (inverse of the frequency, $1/f$)
$\mathbf{T}_n$	Modal period, where n are non-negative integers (inverse of the modal frequency, $1/f_n$)
x	Cross shore distance

CHAPTER 1: INTRODUCTION

Surface gravity waves are an important physical feature of the ocean that affect nearshore processes and contribute to coastal inundation. Fringing reefs protect the shoreline by dissipating wave energy through breaking at the fore reef and additionally through frictional effects and breaking over the reef flat. Reef fringed islands and atolls, for example the Okinawa Islands, Guam and the Republic of the Marshall Islands, have been threatened by inundation due to ocean waves during storm events.

In 1987, a typhoon passing near the Okinawa Islands in Japan caused great coastal damage due to the rise of the water level from a bore-like surf beat (*Nakaza et al.*, 1990). When the waves hit the Okinawa Islands, the waves were more than 5 m higher than normal conditions, damaging the land area near the shoreline (*Nakaza et al.*, 1990). *Nakaza et al.* (1990) related their observations to the excitation of the quarter-wavelength normal mode on the reef flat. Previously, the coral reefs where thought to protect the island from wave energy, which was been proven otherwise from this 1987 typhoon event at the Okinawa Islands.

In 1979, near the Republic of the Marshall Islands a high pressure system was generated, causing the sea level to rise above normal conditions. This also generated storm surge, causing the sea level to rise over 6 m, resulting in an inundation evert on the East coast of Majuro Atoll (*Spennemann*, 1998). This event caused injuries, damage of property, damage of the sewage infrastructure causing approximately 30 million dollars of damage and having nearly 5000 people to be relocated (*Spennemann*, 1998).

There was a potential wave driven inundation event in 2008 at the Republic of the Marshall Islands (*Ford et al.*, n.d.). Unlike the inundation event in 1979, less injuries were reported. Nevertheless, 300 people were relocated due to the damage of properties (*Ford et al.*, n.d.). Damages are thought to be limited due to the low tidal levels during this event (*Ford et al.*, n.d.).

While inundation may occur from different factors including atmospheric disturbances, this research is focused on wave driven inundation, which occurs when four components of the ocean wave field add up to exceed the land elevation. The four components are: high frequency waves (sea and swell), low frequency waves (infragravity), set-up and the tide. Low lying lands are vulnerable to wave driven inundation since small changes in the water level may result in inundation as seen in the Okinawa Islands and the Republic of the Marshall Islands.

The tidal component of the wave driven inundation is as predictable as the tides are due to astronomical forcing with well understood and predictable patterns. The setup is the increase of mean water level due to the breaking of the high frequency waves. Setup on the reef flat is known to decrease during high tide (*Gourlay*, 1996; *Vetter et al.*, 2010), therefore, setup and the tide oppose each other. The elevation of water on the reef flat may be dominated by the setup, as seen during tropical storm Man-Yi over the Ipan reef, Guam (*Péquignet et al.*, 2009). High frequency waves are the waves that people surf and this component on the reef flat is highly correlated with the local water level. The higher the water level on the reef flat, the more high frequency energy is observed on the reef flat (*Vetter et al.*, 2010). Finally the low frequency wave component may be thought of as

the sets or groups of waves that people surf. The low frequency component of wave driven inundation is the topic of this research and will be analyzed in this study.

Field studies and laboratory experiments have been conducted to better understand surface waves and their transformation over reefs (e.g., *Nakaza et al.*, 1990; *Nakaza and Hino*, 1991; *Gourlay*, 1996; *Péquignet et al.*, 2009; *Nwogu and Demirbilek*, 2010; *Vetter et al.*, 2010; *Pomeroy et al.*, 2012; *Péquignet et al.*, 2011; *Van Dongeren et al.*, 2013). Reefs of different forms, lengths, widths and reef flat water depths have been examined in these studies. There have been studies that have focused on the breaking wave setup (e.g., *Gourlay*, 1996; *Nwogu and Demirbilek*, 2010; *Vetter et al.*, 2010; *Van Dongeren et al.*, 2013) and also the high frequency component of the waves, also known as sea and swell waves (*Péquignet et al.*, 2011). There also have been studies that focus on low frequency component of the waves, also known as infragravity waves (e.g., *Nakaza et al.*, 1990; *Nakaza and Hino*, 1991; *Péquignet et al.*, 2009; *Nwogu and Demirbilek*, 2010; *Van Dongeren et al.*, 2013). Prior studies have found that the infragravity waves may be due to the excitation of a quarter-wavelength normal mode over the reef depending on the local water level.

The fringing reefs that have been researched in the past often have a lagoon between the reef flat and the shoreline (*Nwogu and Demirbilek*, 2010; *Pomeroy et al.*, 2012; *Van Dongeren et al.*, 2013). In contrast, for Okinawa, Japan studied by *Nakaza et al.* (1990) and Ipan, Guam studied by *Péquignet et al.* (2009) the reefs are directly attached to the shoreline. This research focuses on the study of infragravity waves and their dynamics over fringing reefs in the Republic of the Marshall Islands directly attached to the shoreline similar to the studies of *Nakaza et al.* (1990) and *Péquignet et al.* (2009).

1.1 INFRAGRAVITY WAVE FIELD STUDIES

Amplification of infragravity waves has been described in terms of open basin normal modes, related to those that are observed over coastal shelves (*Lugo-Fernandez et al.*, 1998). *Lugo-Fernandez et al.* (1998) documented observations of an open basin normal mode over a coastal shelf of 6 km long, on the Tague reef in St. Croix. *Lugo-Fernandez et al.* (1998) concluded from their observations that the quarter-wavelength normal mode is dominant on continental shelves.

Nakaza et al. (1990) spectrally analyzed pressure observations over a reef in the Okinawa Islands during a typhoon event and found a distinctive peak in the low frequency spectrum near the shore. They related this signal to the excitation of the quarter-wavelength normal mode on the reef flat excited by the incident wave groups.

Péquignet et al. (2009) present results from a field study on Ipan reef, an approximately 450 m long fringing reef, on the southeast coast of Guam. This study demonstrated the existence of low frequency modes on the reef during a large wave event due to tropical storm Man-Yi. These modes are not observed on Ipan reef at normal water levels of approximately 0.5 m. *Péquignet et al.* (2009) observed amplification of infragravity waves, as the breaking wave setup increased the water level to approximately 2.0 m over the reef. The increased water depth became the key to the amplified infragravity waves during this wave events.

Nakaza et al. (1990) and *Péquignet et al.* (2009) concluded from their observations that the quarter-wavelength normal mode is dominant on the fringing reef under storm conditions. The quarter-wavelength modal period to which they refer follows the open

basin normal modes and is given by $T_0 = 4L/\sqrt{gh}$, where L is the reef length (cross shore), h is the water depth, and g is the gravitational acceleration (9.81 m/s^2). This equation shows that the modal period depends on the geometry of the reef and the water depth over the reef.

1.2 LABORATORY EXPERIMENTS

Nakaza et al. (1990) also carried out laboratory experiments in addition to the observations made at the Okinawa Islands described above. *Nakaza and Hino* (1991) reported experiments on a reef flat 4.2 m long, and water depth of 0.04 m. By generating irregular incident wave events, *Nakaza et al.* (1990) found that the experimental modes observed were consistent with the theoretical modes with period $T_0 = 4L/\sqrt{gh}$.

Gourlay (1996) studied the setup of waves experimentally by creating idealized reefs comparable to real reefs that are found world wide. In this study, *Gourlay* (1996) found that, the setup increases as the water level on the reef decreases. There was one exception however, on the idealized Guam reef when comparing regular and irregular incident waves in the experiment. The idealized Malé reef showed good agreement of submergence and relative setup when comparing the regular and irregular wave events. However, *Gourlay* (1996) found that the regular and irregular wave events did not agree for the idealized Guam reef. *Gourlay* (1996) hypothesized that this disagreement was possibly due to the excitation of the normal mode on the idealized reef which he did not account for his experiment.

Experiments performed by *Nwogu and Demirbilek* (2010) utilized a typical fringing reef profile from Southeast Guam. Since the experimental setup was a wave flume, *Nwogu and*

Demirbilek (2010) were able to locate sensors at ideal locations and adjust the time the sensors were in use. *Nwogu and Demirbilek* (2010) observed that infragravity energy was low off shore and high on the reef flat. Moreover, the infragravity energy is documented to be lowest at the reef crest and increased shoreward (*Nwogu and Demirbilek*, 2010). *Nwogu and Demirbilek* (2010) spectrally analyzed the data by band averaging 30 frequencies to increase the degrees of freedom and to increase the reliability of the data. *Nwogu and Demirbilek* (2010) also analyzed the raw spectrum for maximum frequency resolution. The raw spectrum for near shore sensors shows the highest infragravity energy at a period of 35 sec, which was consistent with the quarter-wavelength normal mode.

1.3 NUMERICAL MODELING

Recently, researchers have applied numerical models used for coastal shelfs on fringing reefs. Along with the experimental study, *Nwogu and Demirbilek* (2010) also used a nonlinear Boussinesq wave model to futher study wave transformation over a reef. The nonlinear Boussinesq wave model was able to show that the infragravity energy was dominant at the reef flat sensors. *Nwogu and Demirbilek* (2010) found that the model was consistent with the observations made with their experimental setup, period of 35 sec, and they hypothesized that the forcing of the infragravity waves could be due to the energy from the dissipation of the short waves.

Van Dongeren et al. (2013) used the XBeach numerical model to understand the dynamics of the infragravity waves at the Ningaloo reef in Western Australia. Analysis was done both in a one-dimensional and two-dimensional domian. From this study, *Van Dongeren*

et al. (2013) found that for predicting the transformations of the infragravity waves, the two-dimensional model was more accurate. From the model, *Van Dongeren et al.* (2013) found that the amplitude of the infragravity waves are correlated with the water depth over the reef flat. Moreover, the infragravity energy was dominant on the reef flat at Ningaloo reef.

1.4 ALTERNATIVE VIEWS

Although much prior research supports the shelf resonance phenomena on the reef flat, *Pomeroy et al.* (2012) did not see the same phenomena on the Ningaloo reef in Western Australia. The Ningaloo reef is a fringing reef approximately 1.4 km long (*Pomeroy et al.*, 2012). While *Pomeroy et al.* (2012) found that the spectra on the reef flat was dominated by infragravity energy, the observed infragravity wave energy energy was small even when the incident wave was high. A shoreward increase in infragravity wave energy was not observed. Rather, saw that the infragravity wave energy decreased as the wave propagated over the reef flat (*Pomeroy et al.*, 2012). The research by *Pomeroy et al.* (2012) shows that normal modes are not observed over some reef flats, and that further study is necessary in order to understand infragravity energy on the reef flat.

CHAPTER 2: SITE DESCRIPTION

The study site of this research is the Republic of the Marshall Islands, specifically two atolls, Kwajalein Atoll and the Majuro Atoll (Figure 2.1). The Kwajalein array location is referred to as ROI (short for Roi-Namur), and the Majuro array is referred to as CMI (short for College of the Marshall Islands) throughout this research.

The fringing reef that was investigated and where the sensors were placed at ROI is on the northern part of the Kwajalein Atoll in the Roi-Namur area. For CMI, the fringing reef that has been investigated is on the eastern part of the Majuro Atoll near Dalap. Aerial views of both ROI and CMI are shown in Figure 2.2.

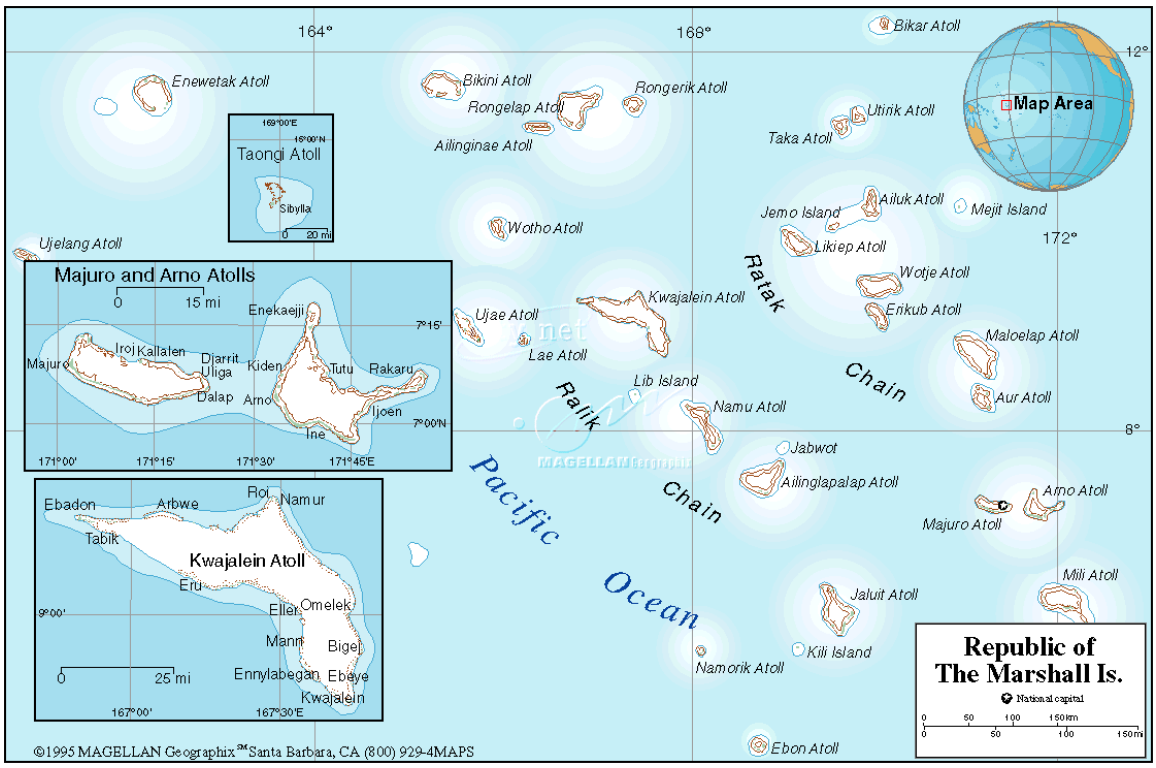

Figure 2.1: Map of the Republic of the Marshall Islands

(a) ROI

(b) CMI

Figure 2.2: Aerial view of ROI and CMI (Google Earth)

The Republic of the Marshall Island was chosen for this research because of the large tidal range in the area. Areas with large tidal range allow us to explore and understand what may happen as water levels vary. Observations over a range of water depths may be used to lend insight into what under future sea level sea level rise scenarios.

Another reason for choosing this location is because the Republic of the Marshall Islands are low lying. The Republic of the Marshall Islands is an area that is vulnerable to inundation and has been exposed to different types of inundation events, including wave driven inundation, an important motivation for this research (*Ford et al.*, n.d.).

CHAPTER 3: DATA

Arrays of cross shore pressure sensors and current meters were deployed across two fringing coral reefs in the Republic of the Marshall Islands. Pressure time series used for this research are described in Table 3.1 and shown in Figure 3.1.

Times series of bottom pressure from three seabird pressure sensors were analyzed for each reef, two located on the reef flat and one located on the fore reef. The fore reef sensor provides measurements of incident wave conditions and is located seaward of the reef crest of the fringing reef at ROI and CMI. The average water depth at the fore reef sensor at CMI is 5.3 m and at ROI is 6.1 m. The reef flat sensors are located midreef and near the shoreline. The pressure sensors at ROI and CMI sample at 1 Hz for 1.5 hours every 3 hours.

Sensor	Reef Length	Average Depth	Position	Location	Start Date	End Date
ROI 1		0.4 m	50 m	Reef flat		5/13/2011
ROI 3	∼300 m	0.7 m	200 m		11/22/2010	4/30/2011
ROI 5		6.1 m	410 m	Fore reef		4/23/2011
CMI 2		0.5 m	44 m	Reef flat		4/10/2011
CMI 4	∼200 m	0.8 m	152 m		11/13/2010	4/17/2011
CMI 7		5.3 m	280 m	Fore reef		3/16/2011

Table 3.1: Information on the reef profile and sensors used in this research. This table provides general information about data used in this research at ROI and CMI.

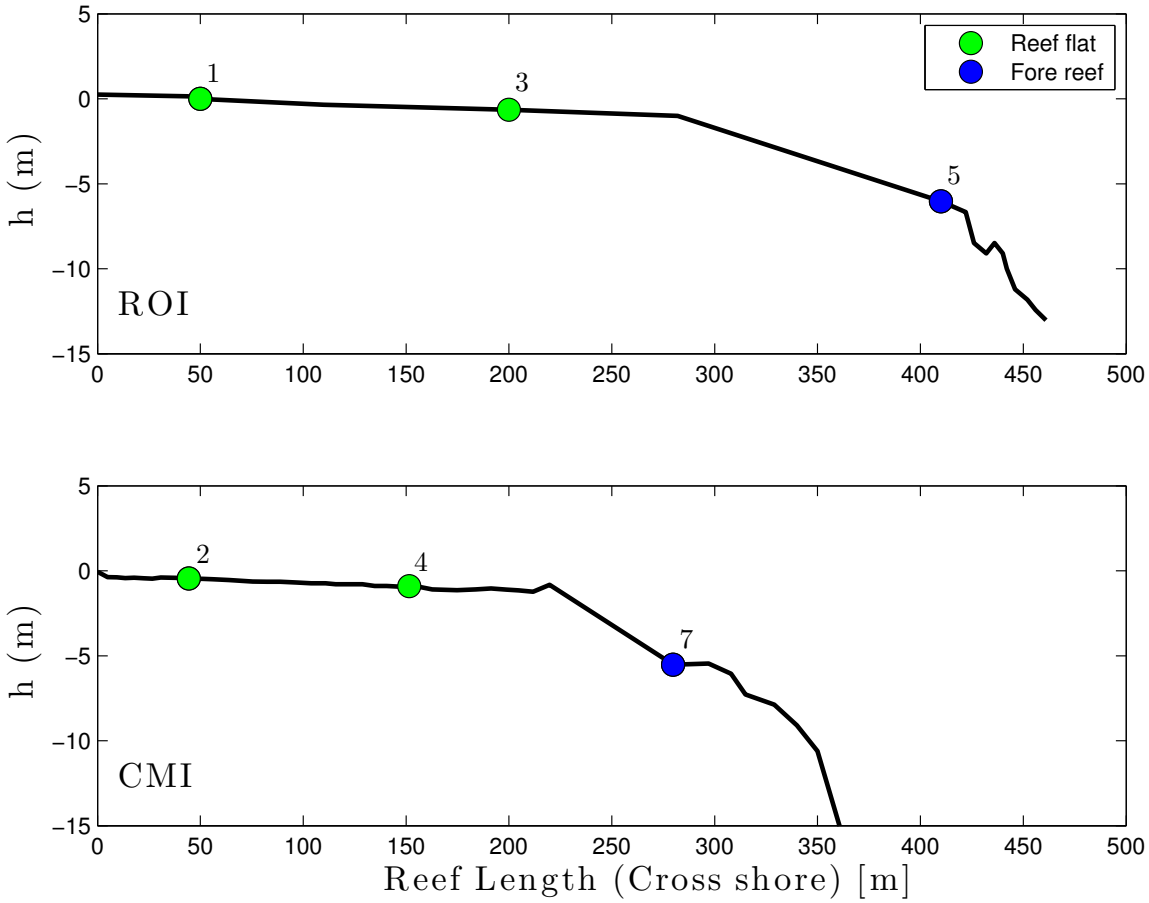

Figure 3.1: Reef profile of (top) ROI and (bottom) CMI with the location of the bottom pressure sensors. There are two sensors on the reef flat and one on the fore reef at each cross shore location. For this research, the three seabird sensors at each reef are used.

CHAPTER 4: METHODS

4.1 WAVE CHARACTERISTICS AND PROPERTIES

A wave may be described by three main length scales; the wave length, the wave height and the local water depth. Figure 4.1 shows a two dimensional general representation of a monochomatic wave.

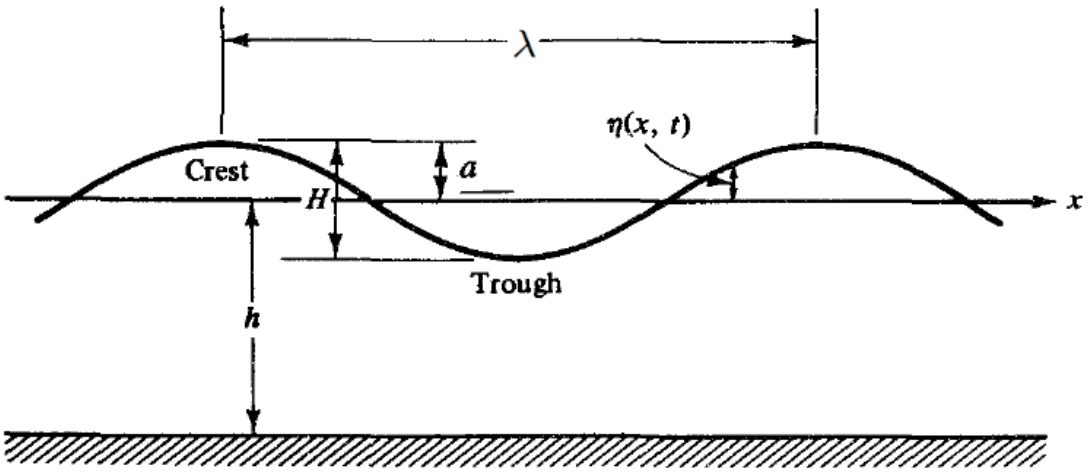

Figure 4.1: Wave properties. This figure shows general parameters in a simple one-dimensional wave. (Figure 1.1 from *Dean and Dalrymple*, 1991)

The wavelength, λ, is the horizontal distance between two crests of a wave, or two troughs of a wave. The wave height, H, is the vertical distance between the crest and the trough of a wave. Another measure of the vertical distance of a wave is the amplitude, a. The amplitude is measured from the mean level of the wave to either the crest or the trough of the wave and $a = H/2$ for a sinusoidal wave. The water depth, h, is measured from the bottom of the ocean floor to the mean level of the wave.

The wave period is given by

$$T = \frac{2\pi}{\omega} = \frac{1}{f} \ , \tag{4.1}$$

where f is the frequency and ω is the angular frequency.

The wave number is expressed as

$$k = \frac{2\pi}{\lambda} \ . \tag{4.2}$$

Finally η is the free surface elevation of the wave which is a function of time and distance. The dynamics of free surface elevation will be further discussed in Section 4.4.

4.2 DISPERSION RELATION

The dispersion relation for linear surface gravity waves of angular frequency ω, is defined by the wave number and water depth, according to

$$\omega = \sqrt{gk \tanh(kh)} \tag{4.3}$$

where g is the gravitational acceleration.

This dispersion relation may be simplified depending on the water depth. The shallowness of water is defined by the relative depth, related to the wavelength λ and the water depth h. Shallow water waves have a large wave length with respect to water depth such that $kh \ll 1$. For instance, when the water depth is 1 km and the wavelength, 20 km the

wave is considered to be in shallow water. Near the shoreline, the water depth is shallow enough that the vertical dependence of the pressure is nearly uniform (Figure 4.2b). As the water depth increases, the vertical dependance of the pressure decays with depth and the water filters out the waves that are shorter in wavelength (Figure 4.2a).

The dispersion relation in shallow water reduces to

$$\omega \approx \sqrt{ghk} \ . \tag{4.4}$$

In the deep water limit, $kh \gg 1$ and the wavelength is much smaller than the water depth. For deep water, the dispersion relation becomes

$$\omega \approx \sqrt{gk} \ . \tag{4.5}$$

The dispersion relationship Equation 4.3 describes the transition zone where deep water waves propagates over an area with decreasing water depth and subsequently into shallow water. The limits of the shallow water, deep water and for intermediate depths defined by *Dean and Dalrymple* (1991) are shown in Table 4.1.

Shallow Water	$kh < \pi/10$	$h/\lambda < 1/20$
Intermediate Depth	$\pi/10 < kh < \pi$	$1/20 < h/\lambda < 1/2$
Deep Water	$kh > \pi$	$h/\lambda > 1/2$

Table 4.1: Definition of shallow, intermediate and deep water limits. (*Dean and Dalrymple*, 1991).

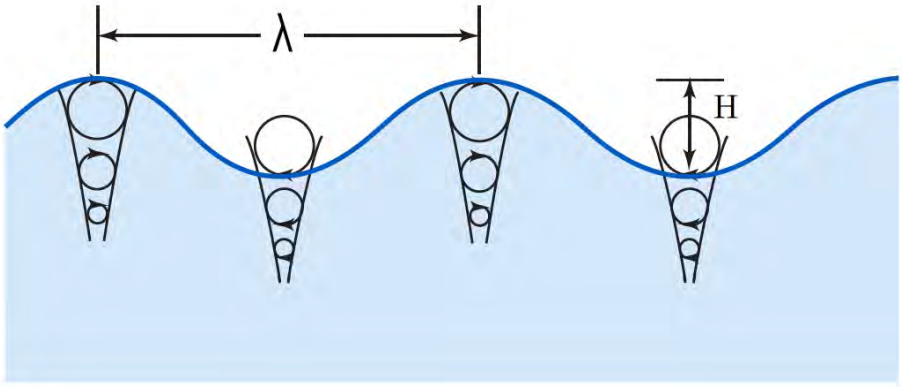

(a) Deep Water

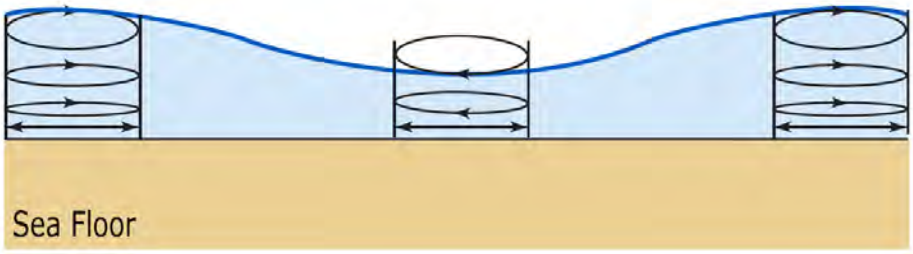

(b) Shallow Water

Figure 4.2: Difference of water particle orbits in deep and shallow water. In deep waters, the water particles beneath the waves are circular and decay with depth. For shallow water, the water particles are elliptically shaped. (Figure 7-4 from *Pinet*, 2009)

To account for intermediate depths, a function was made to solve Equation 4.3 for the wave number k for given water depth, h, and the frequencies, f, of the wave. The function is valid for all depths including the intermediate depths. This function is important to account for the wavelength and water depth when calculating the free surface elevation.

4.3 DATA PROCESSING

For this research, the pressure time series are analyzed using MATLAB® in an effort to relate incident wave energy measured on the fore reef to the energy at the shoreline. The largest observed shoreline response is due to low frequency motions on the reef flat.

The pressure time series are recorded in psi units. First, the raw pressure records are converted to meters. The assumption is made that the atmospheric pressure is constant since atmospheric pressure measurements were not taken concurrently.

Following the conversion, the linear trend and the mean are removed from the data by using the MATLAB® `detrend` function. This is to remove the tide which may be estimated with a linear trend for the 1.5 hour records considered. The mean water level is removed to focus on the dynamic pressure due to waves.

4.4 FREE SURFACE ELEVATION

For all sensors at ROI and CMI, the bottom pressure time series that have been detrended are depth corrected to estimate the free surface elevation. As discussed in Section 4.2, the waves at the shoreline are shallow water waves with pressure uniform in depth. Therefore, the bottom pressure time series is a close estimate to the free surface elevation. On the other hand, for waves in deeper water sites, the bottom pressure time series is no longer a close estimate to the free surface elevation.

For all water depths, the free surface elevation is related to the bottom pressure, P according to

$$\eta = \frac{P}{\rho g K_p(-h)} \ , \tag{4.6}$$

where ρ is the density of water and K_p is the pressure response factor,

$$K_p(-h) = \frac{1}{\cosh(kh)} \ . \tag{4.7}$$

For shallow water $(kh \ll 1) K_p \to 1$ and $\eta = \frac{P}{\rho g}$.

The function to calculate the dispersion relation, presented in Section 4.2, is used to calculate the k, for a given water depth and frequency. Therefore, the pressure response factor may be obtained as a function of frequency at a given sensor location. Since the pressure response factor depends on the frequency, the high frequency range of the waves will be amplified more. For the lower frequencies, the pressure response factor will have less effect on the pressure data.

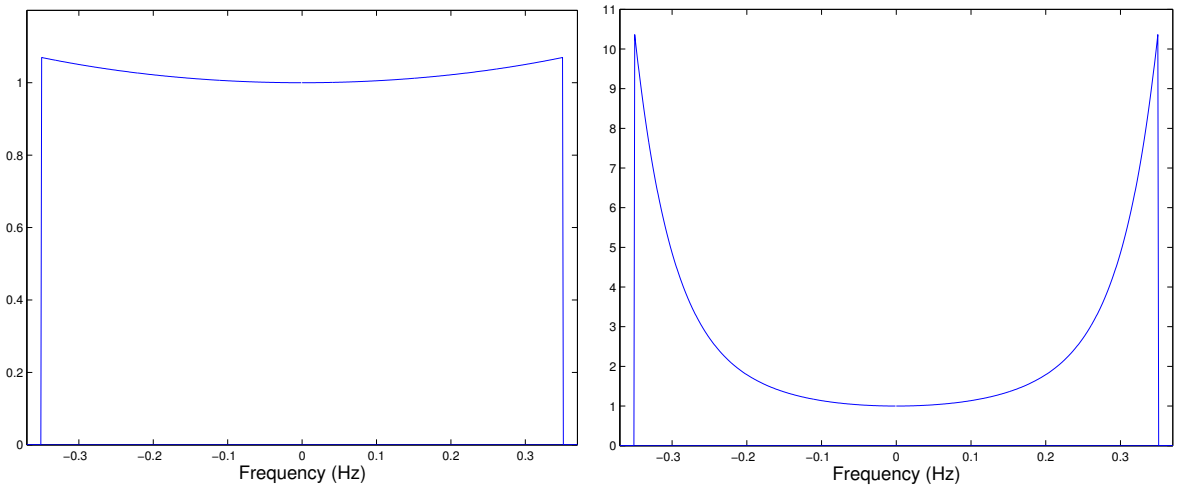

(a) ROI 1 (b) ROI 5

Figure 4.3: The pressure response factor for the bottom pressure time series in the frequency domain for (a) ROI 1 and (b) ROI 5. At ROI 1, the water is nearly depth independent and the pressure response factor is very close to a boxcar filter. At ROI 5, the higher frequencies correspond to waves in intermediate depths with amplitudes that decay with depth.

The pressure response factor is used to depth correct the bottom pressure time series in the frequency domain. Figure 4.3a and 4.3b are the calculated pressure response factor of ROI 1 and ROI 5 respectively. The bottom pressure series in the frequency domain

are multiplied by the pressure response factor to depth correct the data. As one can see in Figure 4.3a, the band pass is nearly uniform as expected for nearly depth independent waves of the reef flat. Also as shown in Figure 4.3b, it is clear that the pressure response factor is much greater for high frequency waves as the deeper locations (Compare to Figure 4.3a).

ROI 1 and CMI 2 are in shallow water; therefore, the depth correction was assumed to be small. However, by applying the depth correction to ROI 1 and CMI 2 it becomes apparent that the depth correction creates slight structure. Therefore to be consistent, the shallow water sensors are also treated with the depth correction factor.

Figure 4.4 shows the progression of the time series of free surface elevation at (a) ROI and (b) CMI across the array. At both ROI and CMI, the figures clearly show there is an overall decrease in the high frequency energy as the wave propagate shoreward. At ROI and CMI, the low frequency component appears to increase shoreward.

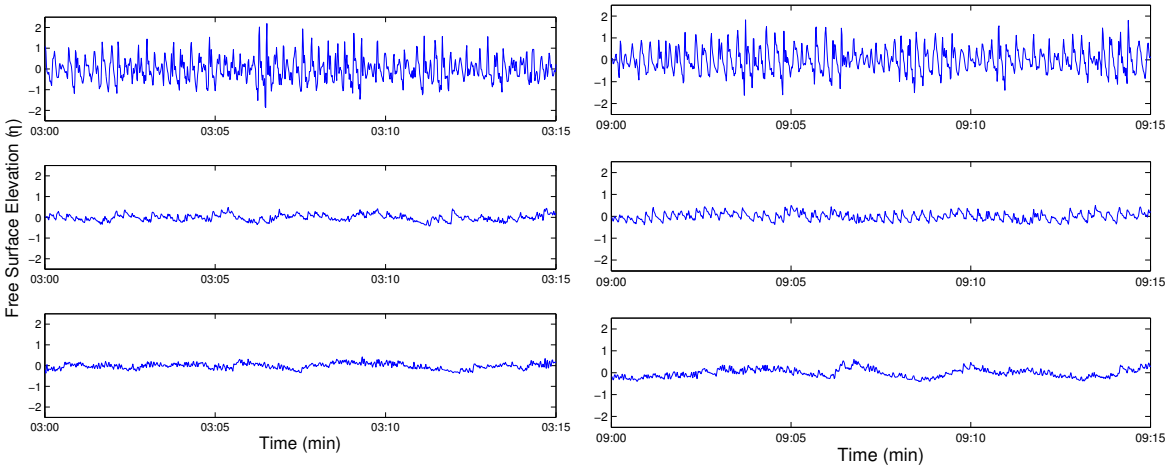

(a) ROI

(b) CMI

Figure 4.4: Fifteen minute free surface elevation time series and its cross shore transition from off shore (top) to shore (bottom) of the free surface elevation at ROI and CMI. The fore reef sensors at ROI and CMI show energetic high frequency motions. The sensors on the reef flat show low frequency motions.

4.5 SIGNIFICANT WAVE HEIGHT

The measured time series are superpositions of waves of different amplitudes and frequencies. Significant wave height is a statistical measure defined as the average of the highest 1/3 waves for a random wave field. For this research, the significant wave height is is calculated by taking the standard deviation of the free surface elevation and multiplying by 4.

Figure 4.5 shows the significant wave height of ROI 1 and ROI 5 on a single figure. Significant wave height of both ROI 1 and ROI 5 have several noticeable peaks. Being relevant to inundation, these high peaks were identified for further analysis.

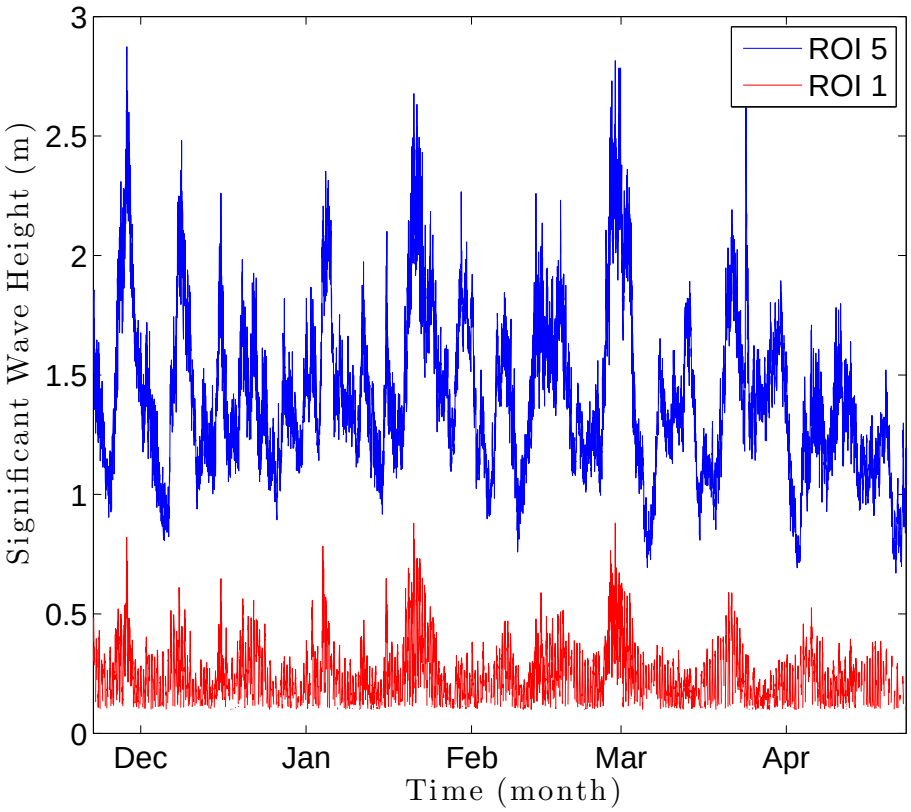

Figure 4.5: Plot of significant wave height at ROI 1 (blue) and ROI 5 (black) against time at ROI. The data with local water depth less than 10 cm are omitted from the analysis. High significant wave height shows energetic events and are the focus of this research.

4.6 BAND PASS FILTER

In order to look at the data in greater detail, the original 1.5 hour pressure time series are reshaped into 900 second records. Similar to the initial data processing, the data is converted into meters and the linear trend is removed. The linear trend here is removed from each 900 second records. Moreover, the significant wave height is estimated for the 900 second record.

To further understand what is generating the high significant wave heights, the free surface elevation is separated into two dynamically different frequency bands. First, the pressure time series is Fourier transformed, and the data is then band pass filtered.

The two dynamically different frequency wave bands are the sea and swell frequency band and the infragravity frequency band. For ROI and CMI, the sea and swell frequency band $1/30 \text{ Hz} < f < 0.35 \text{ Hz}$ includes waves that are driven both by local and distant winds and are energetic on the fore reef prior to wave breaking. The infragravity band $1/900 \text{ Hz} < f \leq 1/30 \text{ Hz}$ includes motions that are energetic on the reef flat. See Appendix A for more information on the sensitivity of the significant wave height estimate due to the change in band width for the sea and swell band and the infragravity band.

A boxcar band pass filter is created (Figure 4.6). After the array for the band pass filter has been created, it is applied to the frequency domain pressure data to eliminate the unwanted frequencies and separate the frequencies into the sea and swell band and the infragravity band.

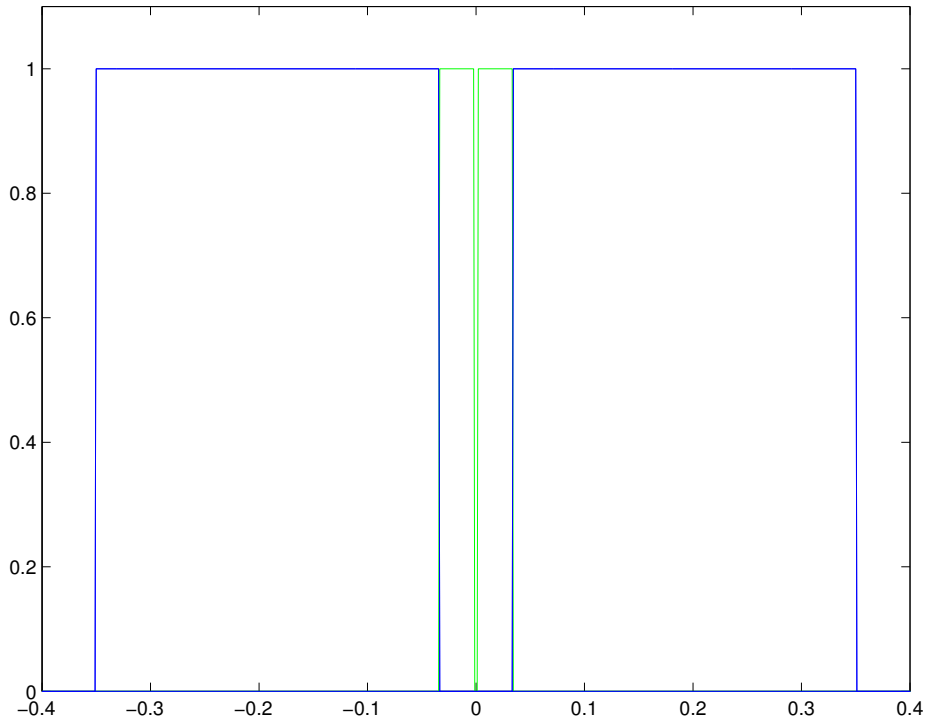

Figure 4.6: A box car band pass filter used for ROI and CMI to separate the two dynamically different frequency bands. Green line shows the low- or infagravity frequency bound and the blue line shows the high- or sea and swell frequency bound.

The upper limit of the sea and swell frequency band is 0.35 Hz. In theory, the highest resolvable frequency should be the Nyquist frequency, in this research 0.5 Hz, due to the sampling rate, 1 Hz. However, due to filtering of short waves by the bottom mounted pressure sensors, the highest resolvable frequency at ROI 5 and CMI 7 is .35 Hz. To accommodate all data sets in different water depths and locations, .35 Hz is used to be the highest resolvable frequency for all the sensors in place of the Nyquist frequency to normalize the data.

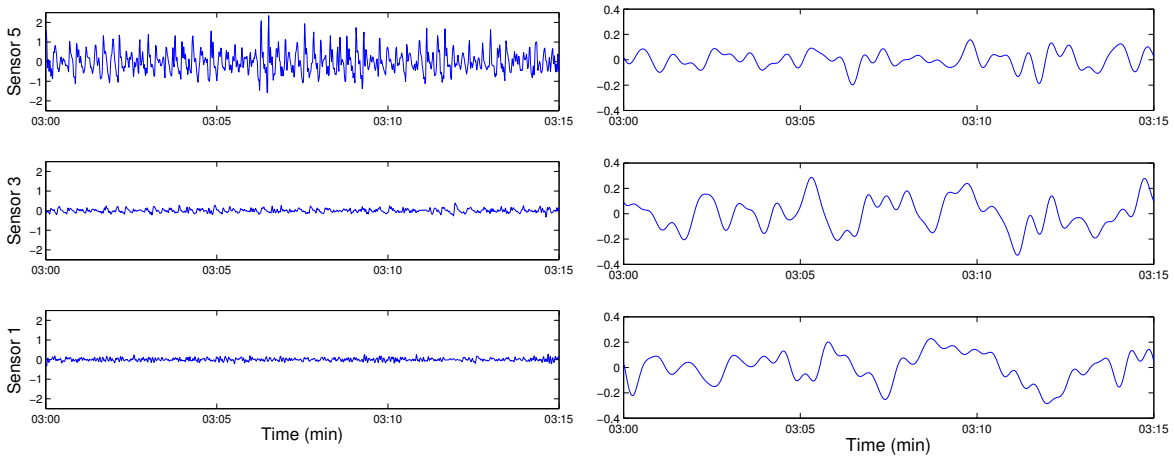

(a) ROI: Sea and Swell (JAN 21, 2011)

(b) ROI: Infragravity (JAN 21, 2011)

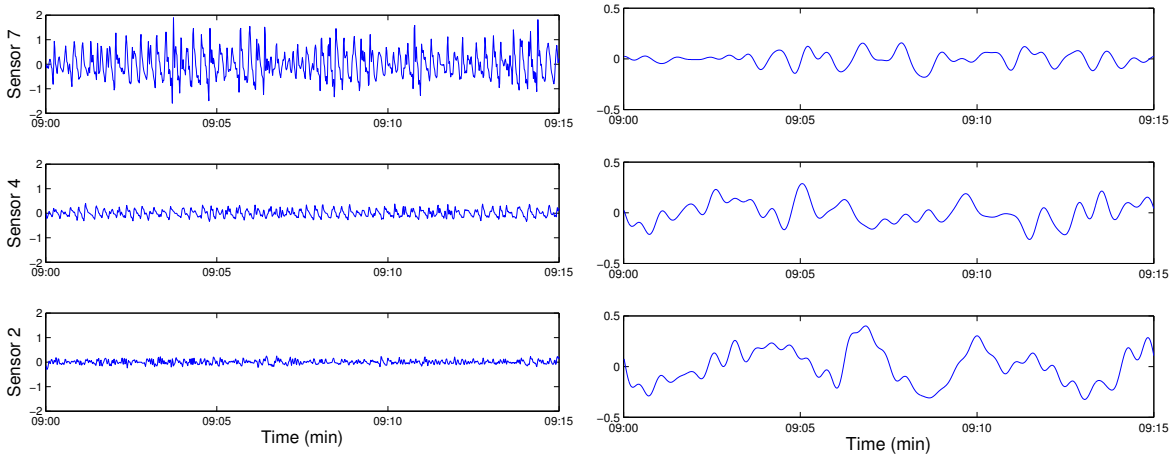

(c) CMI: Sea and Swell (DEC 07,2010)

(d) CMI: Infragravity (DEC 07,2010)

Figure 4.7: Cross shore transformation of the free surface elevation at ROI in the (a) sea and swell frequency band and (b) infragravity frequency band and CMI (c) sea and swell frequency band and (d) infragravity frequency band. At both locations the fore reef sensor shows more energy in the sea and swell band, losing energy as the wave propagates shoreward. The infragravity band shows more energy on the reef flat compared to the fore reef.

4.7 AUTO SPECTRUM

To spectrally analyze the data, the free surface elevation estimated in Section 4.4 is Fourier transformed into the frequency domain. One-sided spectra are calculated, where the negative frequencies are combined with the equivalent positive frequencies. Moreover, there is

no energy at $f > 0.35$ Hz, therefore the high frequency limit for this research, explained in Section 4.5, is 0.35 Hz.

Without averaging the data, the spectral estimates have only two degrees of freedom, thus the statistical reliability of the data is very low. Therefore, both band averaging and ensemble averaging were tested on the spectral estimates to increase the degrees of freedom of the data. For this research, band averaging of the data was found suitable to increase the degrees of freedom to increase the reliability of the data. All of the data is averaged over 5 frequency bands, hence increasing the degrees of freedom to 10 to gain reliability and keep sufficient frequency resolution.

4.8 LOWER FREQUENCY LIMIT

The record length of the data controls the low frequency limit. A longer record length will result in a spectrum where the lower frequencies are better resolved. For ROI and CMI, the lower frequencies were predominantly in the first bin after the mean, $1/T$, when the record is separated in 900 second record lengths. Therefore, analysis is done with the full record length, which is 5400 seconds to increase the lower frequency resolution of the data.

CHAPTER 5: TIME DOMAIN ANALYSIS

The general characteristics of wave transformation over the reefs at ROI and CMI appear similar. The majority of the energy in the free surface elevation is contained in the high frequencies on the fore reef, whereas the free surface elevation on the reef flat near the shoreline is dominated by low frequency energy. Finally, the free surface elevation at mid reef is dominated by the low frequency energy; however, the high frequency energy is larger at mid reef than near the shoreline.

5.1 CROSS SHORE TRANSFORMATION

The transformation of waves from the fore reef to the near shore is shown clearly in Figure 5.1. Figure 5.1a shows that the energy at the fore reef is dominantly in the sea and swell frequencies. The amplitude of the sea and swell energy is much larger compared to the infragravity energy, shown as the solid red line. This figure shows that the infragravity energy is a small contribution to the wave energy at the fore reef.

On the other hand, the infragravity waves are dominant at the shoreline at ROI 1 (Figure 5.1b). In the 900 second wave burst, shown in Figure 5.1b, approximately two oscillations of the infragravity wave are visually present, making the low frequency wave period approximately 7.5 min. Moreover, the amplitudes of the infragravity waves are much larger than those of the sea and swell waves. The sea and swell energy decreases greatly as the wave propagates shoreward, and only provides a small contribution to the total energy near the shoreline.

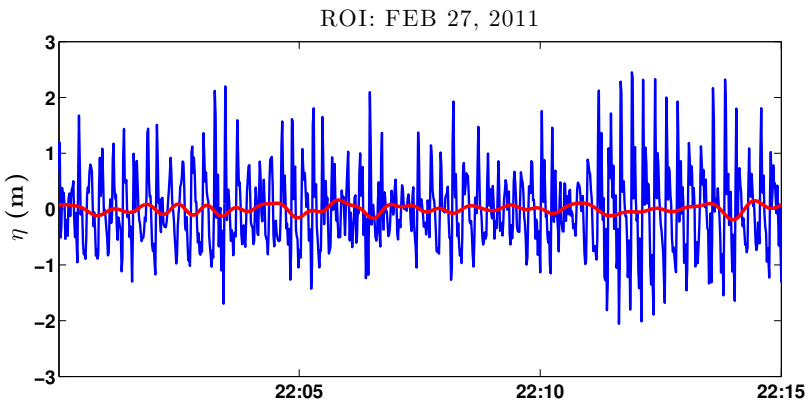

(a) ROI 5

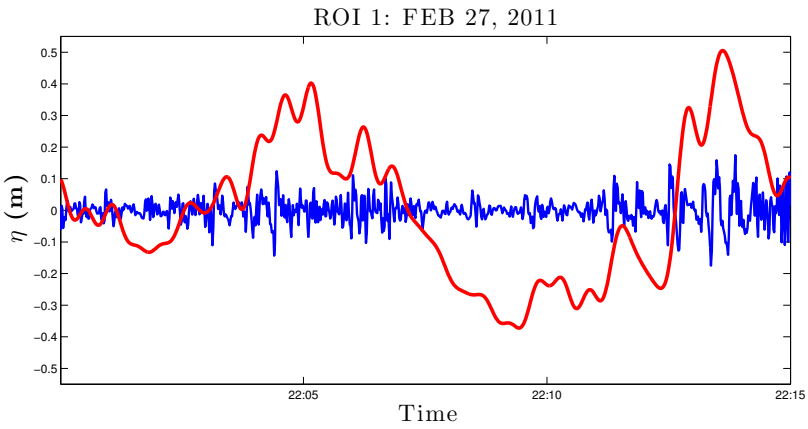

(b) ROI 1

Figure 5.1: Free surface elevation at ROI in two dynamically different frequency bands where the red are the infragravity waves and the blue are the sea and swell waves at (a) ROI 5 and (b) ROI 1. This figure shows that ROI 5 is sea and swell wave dominant, whereas ROI 1 is infragravity wave dominant.

5.2 SIGNIFICANT WAVE HEIGHT

At ROI, eight 1.5 hour time series of high significant wave height have been analyzed spectrally (Figure 5.2a). High significant wave height shows that the wave events are energetic. Also, most of the high significant wave heights at ROI 5 are consistent with the peaks at the shoreline sensor ROI 1. Five 1.5 hour time series of high significant wave height at CMI are analyzed spectrally (Figure 5.3a) during the largest wave events.

Event Name	Record No.	Date
ROI		
ROIe1	302	NOV 28, 2010
ROIe2	769	DEC 08, 2011
ROIe3	1147	DEC 16, 2010
ROIe4	2065	JAN 04, 2011
ROIe5	2635	JAN 16, 2011
ROIe6	2886	JAN 21, 2011
ROIe7	4697	FEB 27, 2011
ROIe8	5873	MAR 24, 2011
CMI		
CMIe1	259	NOV 18, 2010
CMIe2	731	NOV 28, 2010
CMIe3	1875	DEC 22, 2010
CMIe4	3391	JAN 22, 2011
CMIe5	5116	FEB 27, 2011

Table 5.1: High energy events observed at ROI and CMI.

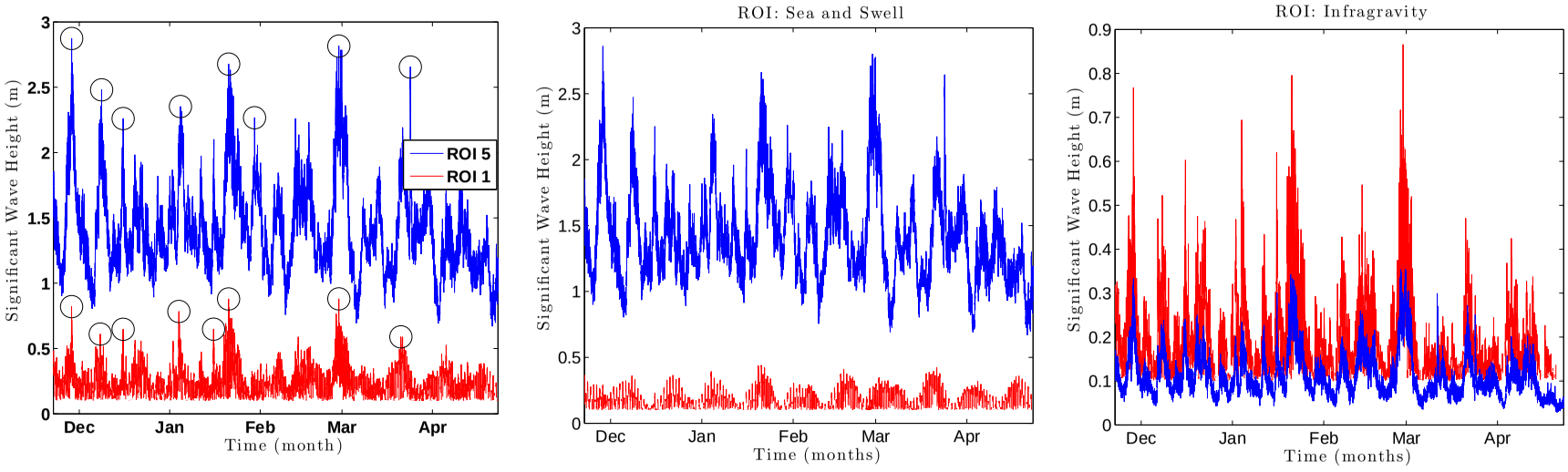

Figure 5.2: Significant wave height at ROI for (a) all frequencies and for (b) sea and swell and (c) infragravity separately. The total significant wave height is used to pick out energetic events to analyze further. The band passed significant wave height shows that the sea and swell energy is always dominant at ROI 5, and the infragravity energy is typically dominant at ROI 1.

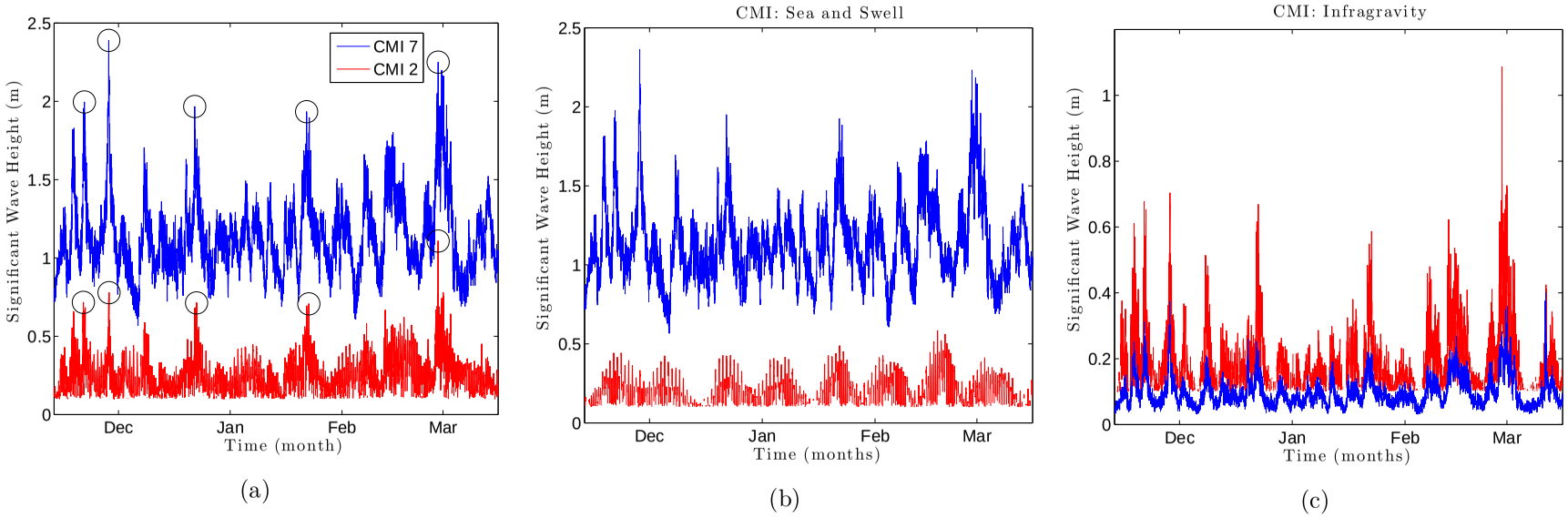

Figure 5.3: Significant wave height at CMI for (a) all frequencies and for (b) sea and swell and (c) infragravity separately. The total significant wave height is used to pick out energetic events to analyze further. The band passed significant wave height shows that the sea and swell energy is always dominant at CMI 7, and the infragravity energy is typically dominant at CMI 2.

Figure 5.2b, 5.2c, 5.3b and 5.3c shows how the sea and swell and the infragravity energy transforms cross shore. These figures show the cross shore transformation over a larger time period compared to Figure 5.1. The sea and swell plots show that there is a lot of energy in the sea and swell frequency band at the fore reef before the waves break. On the other hand, the infragravity bands at ROI and CMI shows that there more infragravity energy on the reef flat compared to the fore reef. These plots show that the sea and swell energy decreases shoreward, and the infragravity energy increases shoreward.

Further, the data are analyzed using scatter plots (Figure 5.5, 5.4 and 5.6). Figure 5.4a is a scatter plot of 15 minute sea and swell significant wave height at ROI on the mid reef versus shoreline, and colored with the local water level. This plot shows that the sea and swell significant wave height is always lower at the shoreline (ROI 1) compared to mid reef (ROI 3). Also the local water level color scale shows that there is more sea and swell energy on the reef flat when there is more water on the reef flat. Therefore, the sea and swell energy is predictable accordingly with the water level on the reef flat (Figure 5.5a). This also is true at CMI. Figures 5.4b and 5.5b are equivalent to Figures 5.4a and 5.5a, but only with the data collected at CMI. The two figures are very similar, and they both show that the sea and swell energy decreases shoreward on the reef flat, and that sea and swell wave height at the reef flat is an increasing function of water level.

On the other hand, the scatter plot of the infragravity energy at the shoreline versus mid reef shows that there are times when the energy increased shoreward on the reef flat, at both at ROI and CMI (Figure 5.6a and 5.6b). Both at ROI and CMI, the infragravity energy increased shoreward on the reef flat when the local water level was high. The effect

of local water level on the infragravity energy is less evident than for the sea and swell, however, higher water levels on the reef flat do allow more infragravity energy to reach the shoreline. This does not mean that the infragravity waves are always large when the water level is high. There are events that show high local water level but the infragravity energy at ROI 1 and CMI 2 are lower than seen at ROI 3 and CMI 4.

For the infragravity energy, the scatter plot is also presented colored with the significant wave height at the fore reef sensors (Figure 5.6). These plots show the relation of the energy distribution on the reef flat depending on the energy seen on the fore reef. These plots show that both at ROI and CMI, the infragravity energy content on the reef flat depends on the energy at the fore reef sensor. Typically, more energy seen on the fore reef results in more infragratity energy on the reef flat.

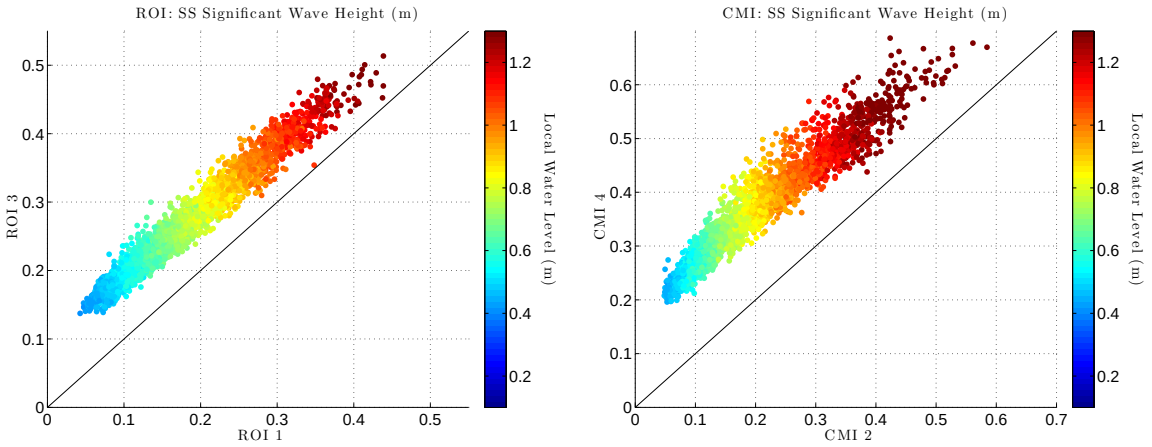

(a) ROI SS: Comparing reef flat sensors

(b) CMI SS: Comparing reef flat sensors

Figure 5.4: Scatter plots of sea and swell wave heights at the shoreline sensor versus the mid reef sensor at (a) ROI and (b) CMI colored by local water level showing that sea and swell energy decays shoreward. Observations $h < 0.1$ m are omitted fro this analysis.

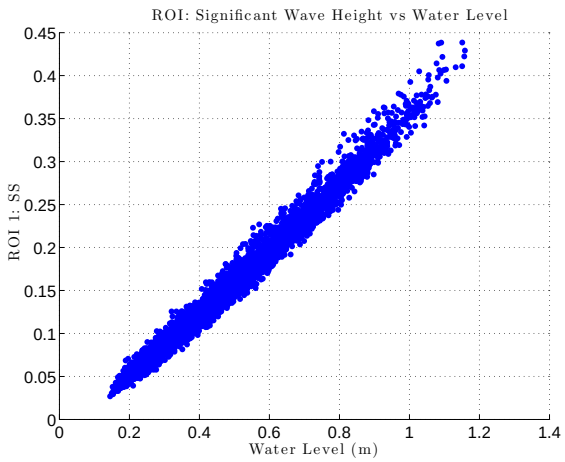

(a) ROI SS: Comparing reef flat sensors

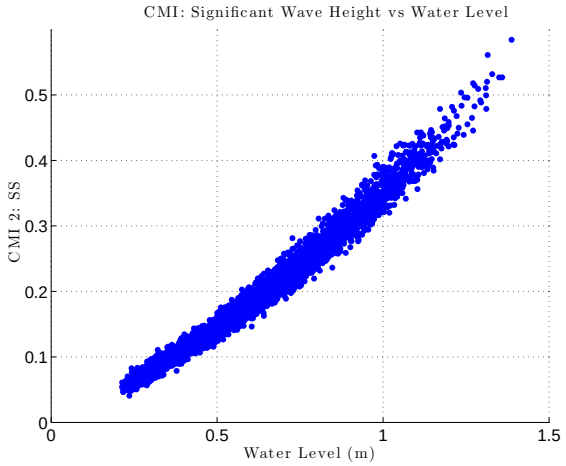

(b) CMI SS: Comparing reef flat sensors

Figure 5.5: Scatter plots of shoreline sea and swell wave heights at (a) ROI and (b) CMI versus local water level. This figure shows clearly that the sea and swell waves, both at ROI and CMI are highly correlated with the local water depth.

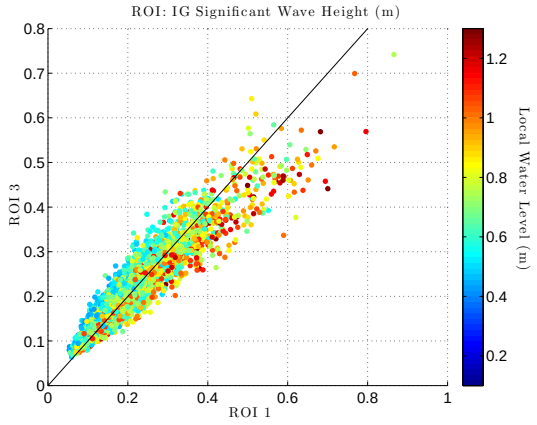

(a) ROI IG: Local Water Level

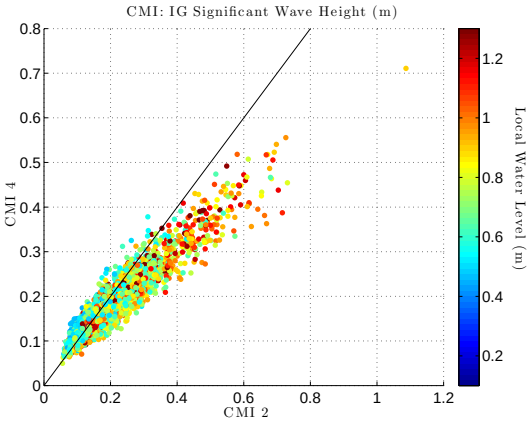

(b) CMI IG: Local Water Level

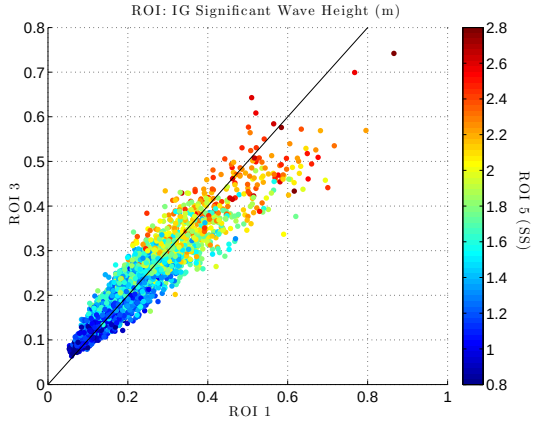

(c) ROI IG: Significant Wave Height ROI 5

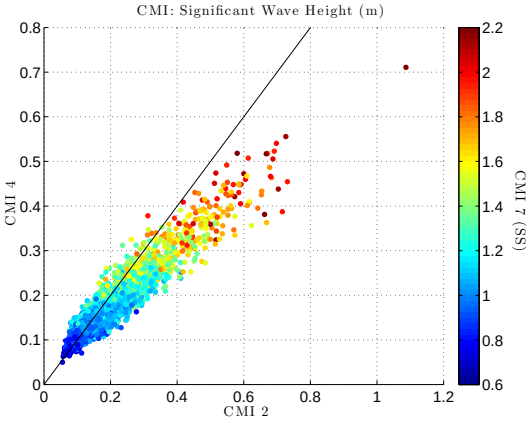

(d) CMI IG: Significant Wave Height CMI 7

Figure 5.6: Scatter plots of infragravity waves over the reef flat sensors at (a, c) ROI and (b, d) CMI. Figures show the relation with the (a, b) local water level or (c, d) the energy at the fore reef compared to the energy at the reef flat depending on the location of the sensors in the infragravity frequency band.

CHAPTER 6: WAVE DYNAMICS

6.1 LONG WAVE EQUATIONS: NORMAL MODES

On the reef flat, shallow water waves are also known as long waves. The free surface elevation of a shallow water wave obeys the wave equation,

$$\frac{\partial^2 \eta}{\partial t^2} = c^2 \frac{\partial^2 \eta}{\partial x^2} \ , \tag{6.1}$$

where the speed of waves is $c^2 = gh$, t is the time and x is the cross shore direction.

When the time dependance of η as expressed as a complex exponential,

$$\eta = \hat{\eta}(x) e^{i\omega t} \ , \tag{6.2}$$

we find that the wave equation becomes an ordinary differential equation for the spatially dependant amplitude of the free surface elevation

$$\frac{d^2 \hat{\eta}}{dx^2} + \frac{\omega^2}{gh} \hat{\eta} = 0 \ . \tag{6.3}$$

Equation 6.3 is solved given the boundary conditions of $\frac{d\eta}{dx} = 0$ at $x = 0$, and $\eta = 0$ at $x = L$ (Figure 6.1).

The general solution of Equation 6.3 is,

$$\eta = A \cos(kx) + B \sin(kx) \ . \tag{6.4}$$

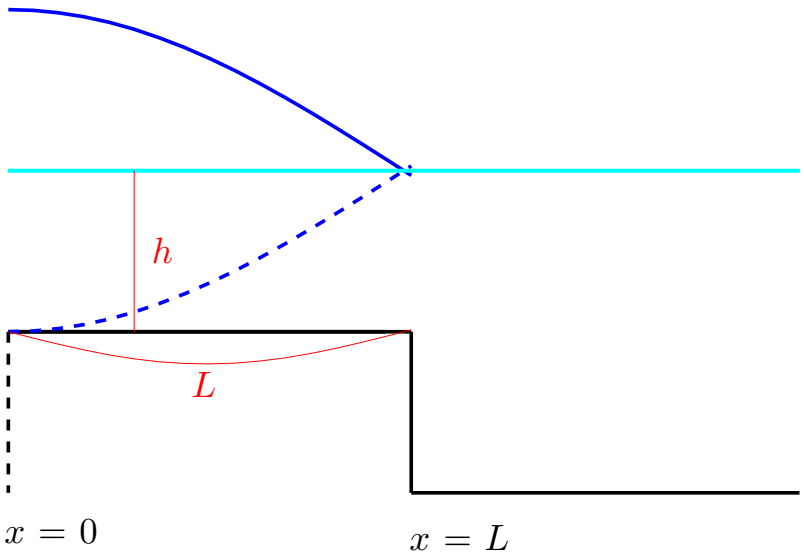

Figure 6.1: Standing wave in an idealized reef where h is the water depth and L is the cross shore reef length.

At the antinode, where $x = 0$, $\frac{d\eta}{dx} = 0$, we find that $B = 0$. At the node, where $x = L$, $\eta = 0$, we find that $\eta = A\cos(kL) = 0$; hence, $k_n L = \frac{(2n+1)\pi}{2}$.

The solution of Equation 6.3 and the boundary conditions is

$$\hat{\eta} = A\cos\frac{(2n+1)\pi}{2L}x \ . \tag{6.5}$$

The dispersion relation of long waves relate the frequency and wave number,

$$\omega_n = \sqrt{gh}k_n \tag{6.6a}$$

which may be rearranged to yield,

$$k_n = \frac{\omega_n}{\sqrt{gh}} \ . \tag{6.6b}$$

In Equation 6.5, k_n is shown to be equal to $\frac{(2n+1)\pi}{2L}$. From this and applying the dispersion relation,

$$k_n = \frac{(2n+1)\pi}{2L} = \frac{\omega_n}{\sqrt{gh}} \ . \tag{6.7}$$

or

$$\omega_n = \sqrt{gh}\frac{(2n+1)\pi}{2L} \tag{6.8}$$

The angular frequency is related to the period of oscillation,T, according to

$$\omega = \frac{2\pi}{T} \tag{6.9}$$

hence

$$T_n = \frac{4L}{(2n+1)\sqrt{gh}} \ . \tag{6.10a}$$

Letting $n = 0$, the period of the gravest mode, T_0, is

$$T_0 = \frac{4L}{\sqrt{gh}} \ . \tag{6.10b}$$

CHAPTER 7: SPECTRAL ANALYSIS

By computing the auto spectra of different wave bursts during events with enhanced infragravity energy on the reef flat, we find the observed frequency and spatial structure are consistent with that of the gravest normal mode.

7.1 CROSS SHORE TRANSFORMATION

The cross shore transformation of the wave field shows energetic sea and swell at the fore reef sensor that decays shoreward. Infragravity waves may be more energetic than the depth limited sea and swell waves on the reef flat. Figure 7.1a is a log-log plot of the spectral density of a 1.5 hour wave burst at ROI on February 27th, 2011. This figure shows this cross shore transformation is consistent with the time domain analysis if Section 5.1. ROI 5 shows that the fore reef energy is largest in the sea and swell band. The energy in the infragravity band at the fore reef sensor is significantly smaller than the energy in the sea and swell band. The reef flat sensors, ROI 1 and 3, show a spectral peak frequency is at 3.15×10^{-3} Hz ($T_0 = 318$ sec). There is more energy at the peak frequency at ROI 1, the closest to the shoreline compared to ROI 3 on the mid reef consistent infragravity energy increasing shoreward (Section 5.1 and Figure 5.1b).

The observations made at CMI are consistent with the observation at ROI. The spectral transformation of Figure 7.1b is similar to Figure 7.1a. Again, at CMI 7, there is more energy in the sea and swell band than in the infragravity band. Moreover, the peak frequencies at CMI 4 and CMI 2 are 2.22×10^{-3} Hz ($T_0 = 450$ sec) and the amplitude of this spectral peak

also is increasing shoreward. Again, this is consistent with observed increase in infragrativy energy shoreward presented in Section 5.1 and Figure 5.1b.

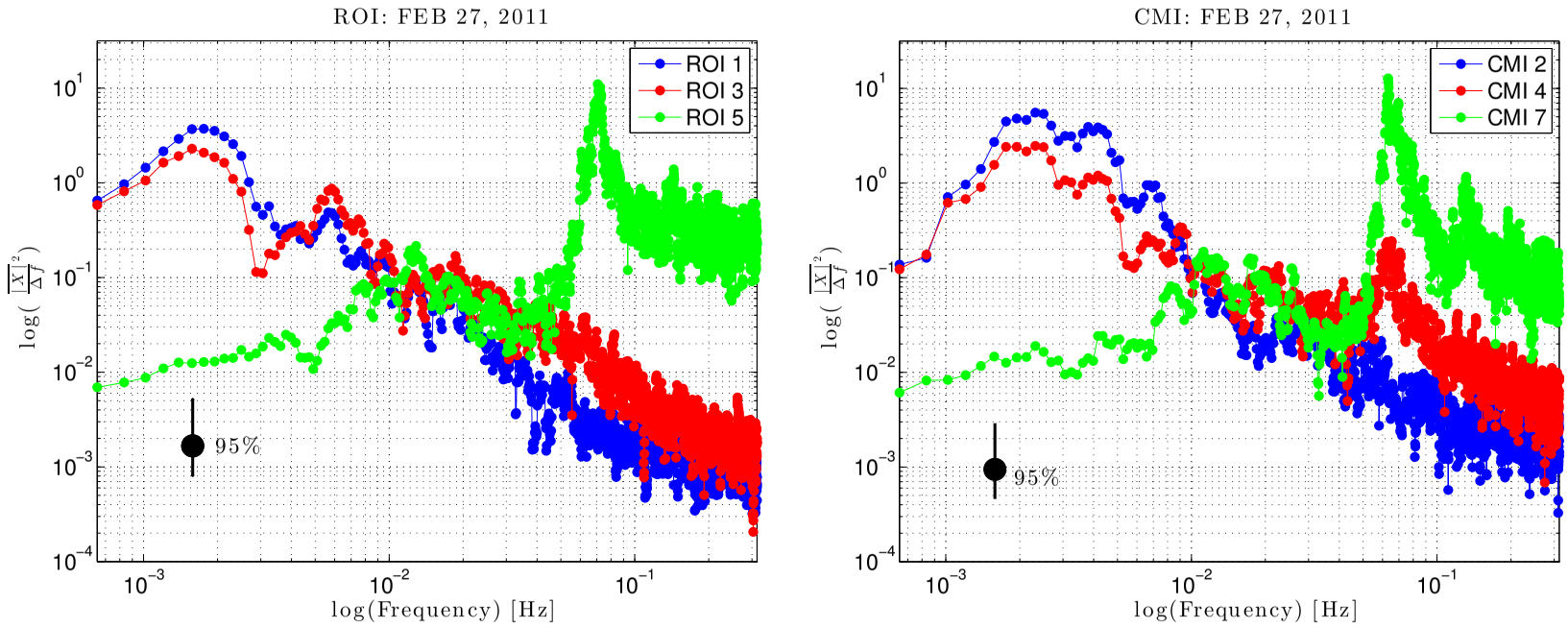

(a) ROI (b) CMI

Figure 7.1: Spectral density of cross shore transformation of wave energy at (a) ROI and (b) CMI where the green line is the fore reef sensor, the red line is the mid-reef sensor and the blue line the near shore sensor plotted on a log-log scale. These figures are band averaged with 10 degrees of freedom. At both ROI and CMI the reef flat sensors have more energy in the infragravity wave bands, where the sensor on the shoreline being more energetic. On the other hand, the fore reef sensors have more energy in the sea and swell wave band, and little energy in the infragravity wave band.

7.2 EFFECT OF WATER LEVEL

In this section, we examine water level effects on the observed peak frequency of the waves on the reef flat. Equation 6.10 shows that the water depth, h, on the reef flat affects the peak frequency. At ROI, three 1.5 hour time series with average reef water levels (defined as the average water level at the shoreline and the mid reef sensors) of 0.64 m, 0.93 m and 1.2 m are examined spectrally. Figure 7.2a is a plot of the spectral density of the free surface time series for the different water levels. At 1.2 m water level, the observed peak frequency is at 3.06×10^{-3} Hz ($T_0 = 327$ sec). At 1.0 m, the observed peak frequency is 2.50×10^{-3} Hz ($T_0 = 400$ sec). Finally at 0.64 m, the peak frequency is at 1.76^{-3} Hz ($T_0 = 480$ sec). The observed decrease in peak frequency with water depth is consistent with Equation 6.10.

Similar to ROI, at CMI the observed spectral peak frequency increases as the water level increases (Figure 7.2b). When the water level dependance is plotted at CMI, the peak frequency at water level 1.2 m is 3.80×10^{-3} Hz ($T_0 = 263$ sec). At water level 1.0 m, the peak frequency is at 3.61×10^{-3} Hz ($T_0 = 277$ sec). Finally at water level 0.91 m the peak frequency is 2.31×10^{-3} Hz ($T_0 = 432$ sec), again consistent with Equation 6.10.

Table 7.1 also includes the theoretical peak period of the gravest mode calculated from $T_0 = 4L/\sqrt{gh}$. The theoretical peak period is similar to the observed peak period. Sources of error in T_0 are discussed in Appendix B. The dependance of theoretical period, on the water level is consistent with the observations. Both at ROI and CMI, the peak period is smaller when the water level on the reef flat is higher consistent with, $T_0 \propto 1/\sqrt{gh}$ (Equation 6.10).

Record No.	Date	Water Level (m)	Observed Peak Frequency ($\times 10^{-3}$ Hz)	Observed Peak Period (sec)	Theoretical Peak Period (sec)
Constant reef length of $\sim$ 300 m (ROI)					
2886	JAN 21, 2011	1.2	3.06	327	350
302	NOV 28, 2010	1.0	2.50	400	383
4697	FEB 27, 2011	0.64	1.76	568	480
Constant reef length of $\sim$ 200 m (CMI)					
1875	DEC 22, 2010	1.2	3.80	263	219
731	NOV 28, 2010	1.0	3.61	277	260
259	NOV 18, 2010	0.91	2.31	432	279

Table 7.1: Observed peak frequency and period from the spectral analysis described in Section 7.2 compared with the theoretical peak period (Equation 6.10).

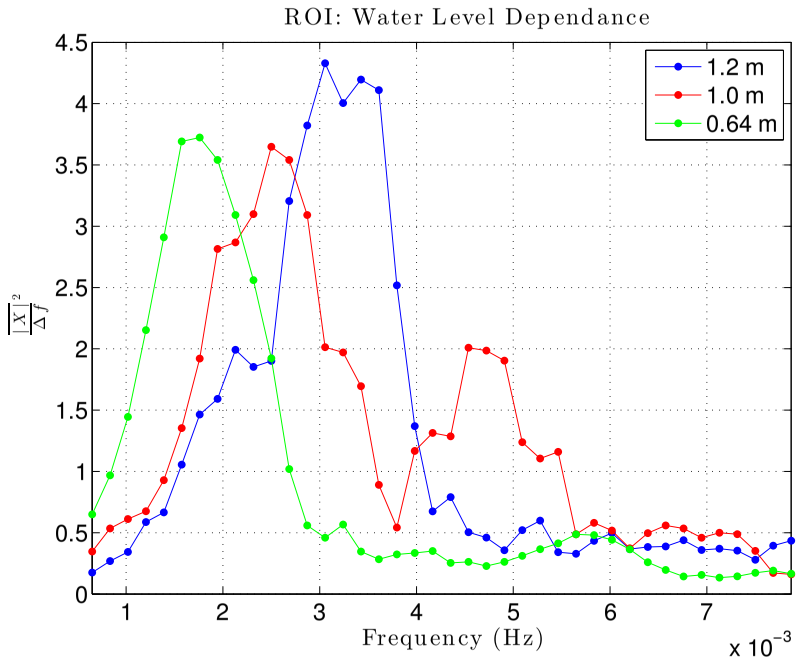

(a) ROI with different water levels. Blue at 1.2m, red at 0.93m and green at 0.64 m.

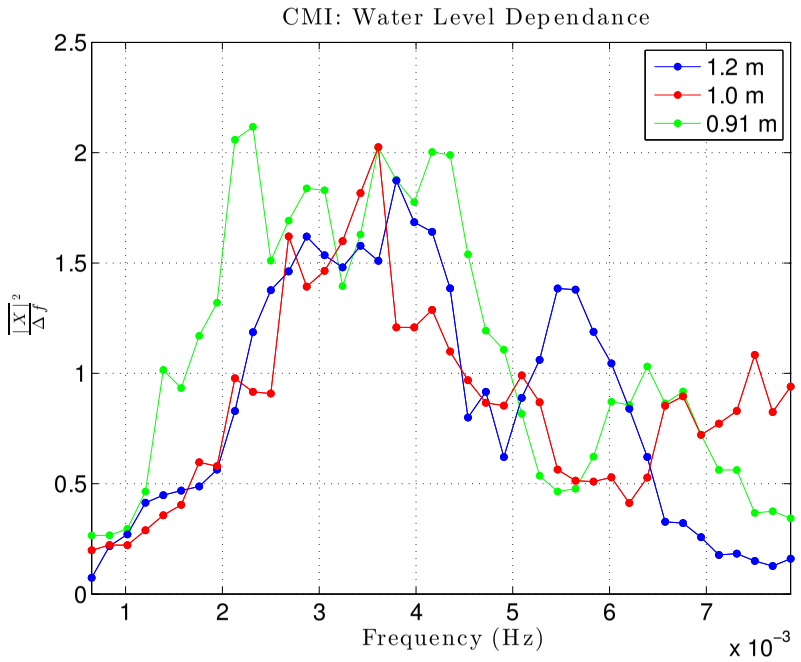

(b) CMI with different water levels. Blue at 1.2m, red at 1.0m and green at 0.90 m.

Figure 7.2: Effect of water level on peak frequency. Auto spectra of the free surface elevation at the shoreline at (a) ROI and (b) CMI for reef flat water level of (blue) ∼1.2 m and (red) ∼1.0 m and (green) ∼0.64 m at (a) ROI and ∼0.91 m at (b) CMI. Note how the peak frequency at higher water levels are higher than at lower water levels.

7.3 EFFECT OF REEF LENGTH

ROI and CMI are both fringing reefs but with different reef lengths. ROI has a reef length of approximately 300 m and CMI has a reef length of approximately 200 m. The peak frequency at ROI is lower compared to CMI for similar reef flat water levels. Figure 7.3a shows a plot of the spectral density of ROI and CMI for a 1.5 hour free surface elevation time series when the water level was approximately 1.0 m. The peak frequency at ROI is 2.50×10^{-3} Hz ($T_0 = 400$ sec). Comparing the peak frequency to the peak frequency at CMI, 3.61×10^{-3} Hz ($T_0 = 260$ sec), shows that the peak frequency is located at a higher frequency compared to ROI.

At approximately 1.2 m water level (Figure 7.3b), we find that the observed peak frequency at ROI 1 is 2.69×10^{-3} Hz ($T_0 = 356$ sec). At CMI 2, the observed peak frequency is 3.80×10^{-3} Hz ($T_0 = 219$ sec). The larger observed peak period at ROI 1 versus CMI 2 is consistent with the reef length at ROI being larger than the reef length at CMI. These findings show that the peak frequency is dependent on the geometry of the reef structure, specifically the length of the reef. For the same reef flat water level, shorter reef have smaller peak periods.

Moreover, the reef length ratio of the reef length at ROI to CMI (300 m/200 m) is 1.5, and the observed peak periods also follow this ratio. In approximately 1.0 m depth, the ratio is 400 sec/ 260 sec $\sim$1.5. In 1.2 m depth, the ratio is 356 sec/ 219 sec $\sim$1.6.

Table 7.2 also includes the theoretical peak period calculated from $T_0 = 4L/\sqrt{gh}$. Again, similar to Section 7.2 the theoretical peak period is similar to the observed peak period (See Appendix B for errors).

Record No.	Date	Reef Length (m)	Observed Peak Frequency ($\times 10^{-3}$ Hz)	Observed Peak Period (sec)	Theoretical Peak Period (sec)
Water level $\sim$ 1.0 m					
302	NOV 28, 2010	$\sim$ 300 (ROI)	2.50	400	383
731	NOV 28, 2010	$\sim$ 200 (CMI)	3.61	277	260
Water level $\sim$ 1.2 m					
2065	JAN 04, 2011	$\sim$ 300 (ROI)	2.69	372	356
1875	DEC 22, 2010	$\sim$ 200 (CMI)	3.80	263	219

Table 7.2: Observed peak frequency and period from the spectral analysis described in Section 7.3 compared with the theoretical peak period (Equation 6.10).

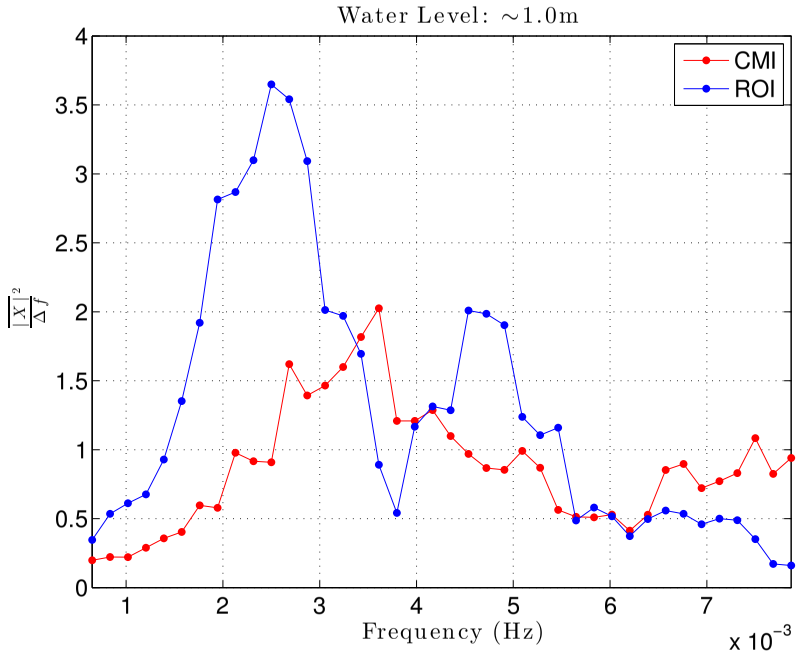

(a) Effect of change in reef length at ∼ 1.0 m water level

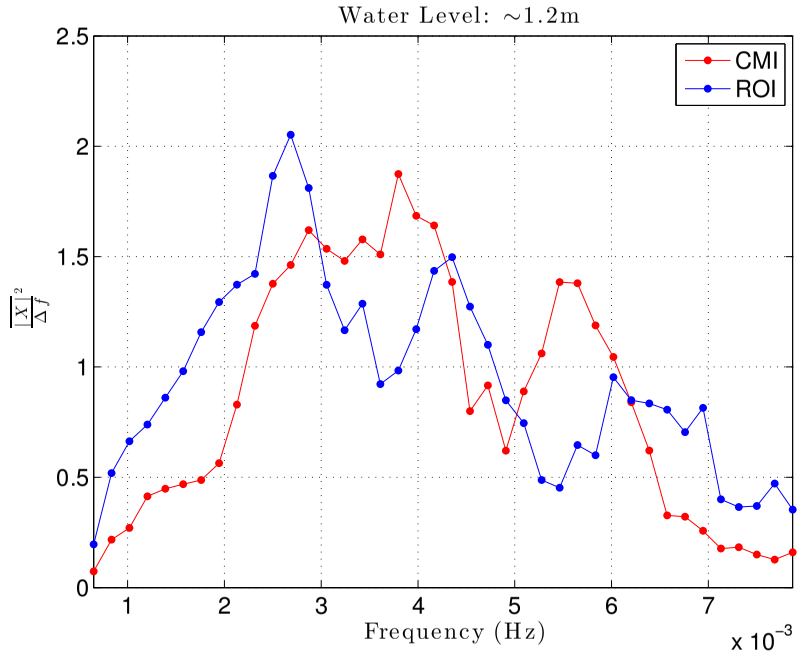

(b) Effect of change in reef length at ∼ 1.2 m water level

Figure 7.3: Effect of reef length on peak frequency. Auto spectra of the free surface elevation at the shoreline at (red) CMI and (blue) ROI for reef flat water level of (a) ∼1.0 m and (b) ∼1.2 m. Note how the peak frequency at ROI is lower than at CMI for a given water level consistent with the larger reef length at ROI.

7.4 REEF FLAT TRANSFORMATION

By comparing different time series across the reef flat at ROI and CMI, we are able to see how the infragravity energy transforms over the reef flat. At ROI 1 and ROI 3, when the time series are spectrally analyzed, the spatial structure of the infragravity energy is clear. Figure 7.4 shows the auto spectra for four 1.5 hour time series at ROI to compare the amount of energy near the observed peak frequency at the shoreline (ROI 1) and mid reef (ROI 3). The figures makes it clear that ROI 1 always has more energy near the observed peak frequency compared to ROI 3. This is consistent with our results for Section 7.1 with infragravity energy increasing shoreward and also from Equation 6.5 ($n = 0$) that describes the spatial structure of the quarter-wavelength normal mode.

Figure 7.5 also shows four 1.5 hour time series spectrally analyzed, at CMI 2 and CMI 4. These figures show consistency with ROI, where the energy of the infragravity near the observed peak frequency at CMI 2 is larger compared to CMI 4. This again is consistent with what we expect to see in the quarter-wavelength normal mode (Equation 6.5, $n = 0$). As the wave gets closer to the shoreline, the infragravity energy is larger than at the mid reef sensors.

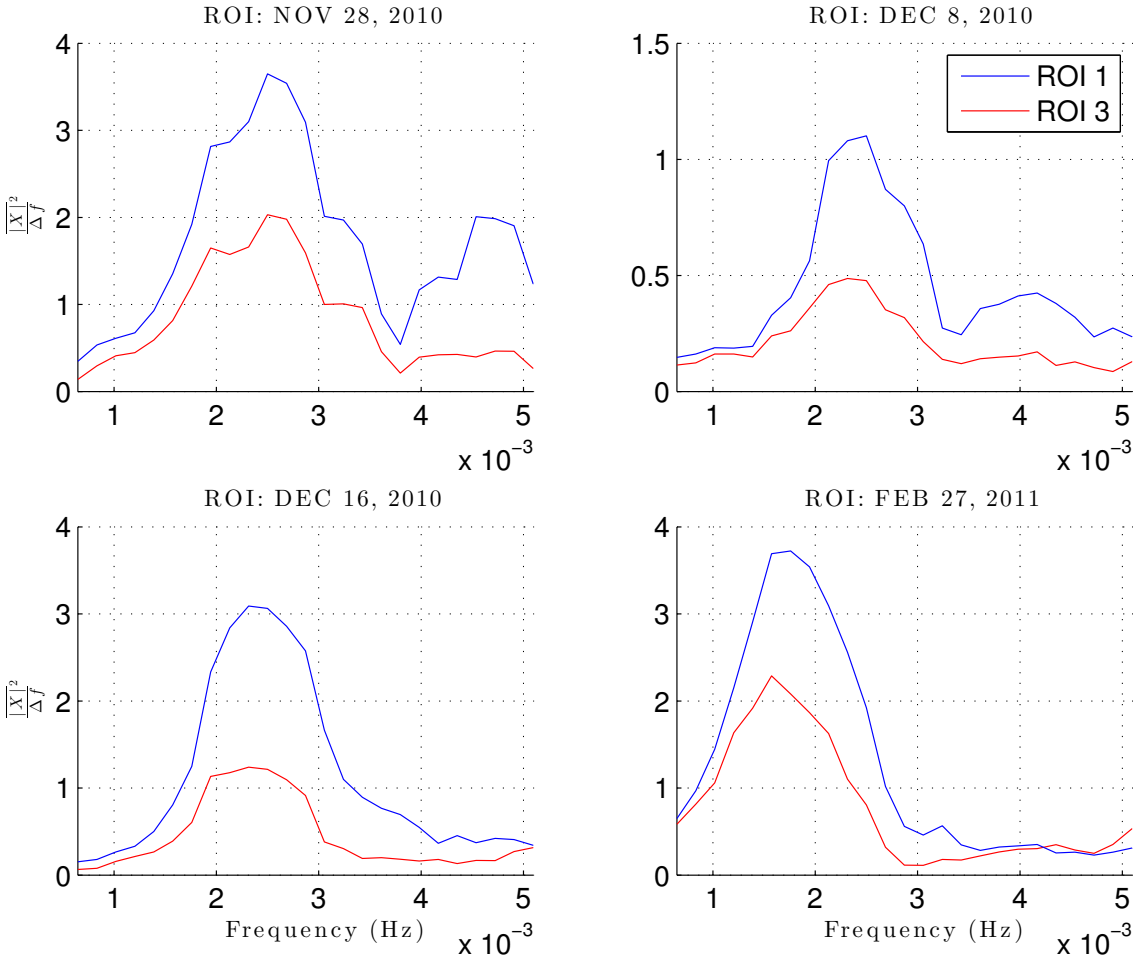

Figure 7.4: Auto spectra at (blue) ROI 1 and (red) ROI 3 for four time series (ROIe1, ROIe2, ROIe3, ROIe7). This figure shows that at the observed peak frequency, the energy at ROI 1 is always greater than at ROI 3. This is also consistent with the normal mode theory where the energy of the infragravity wave increases shoreward.

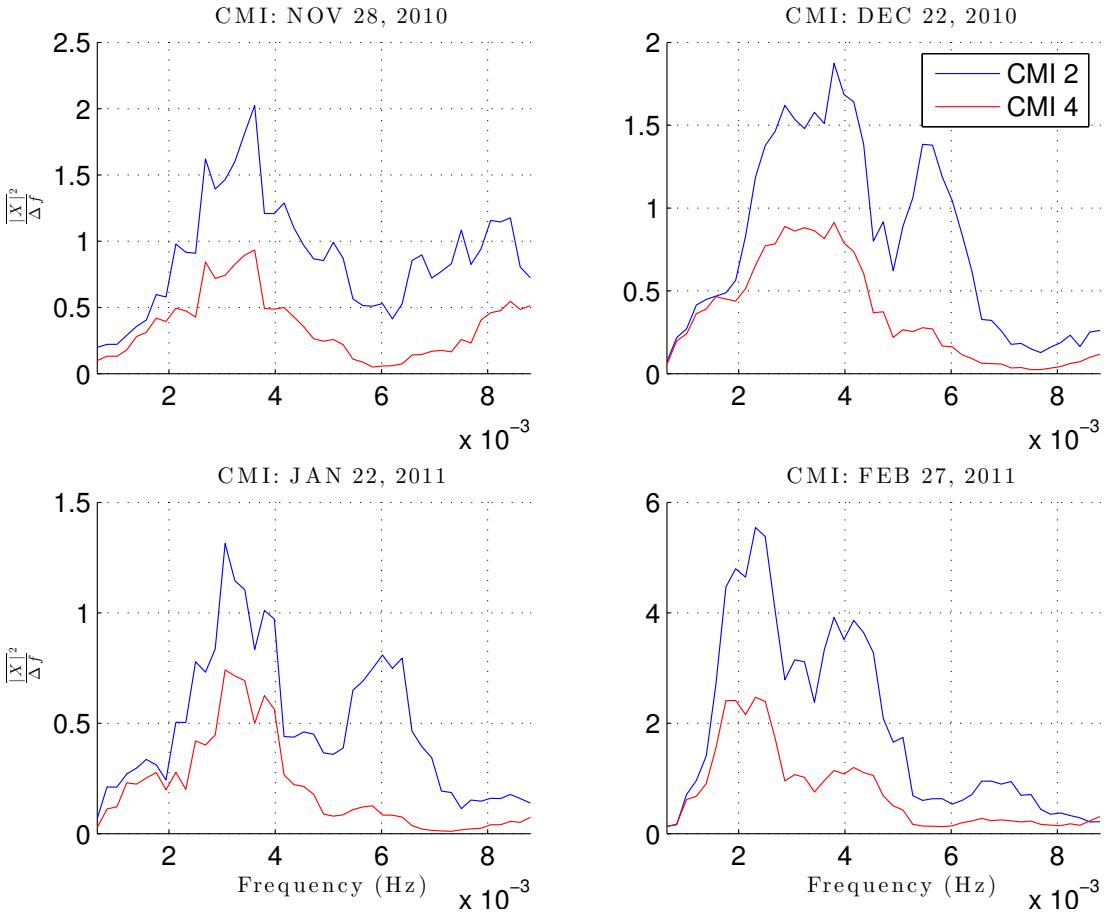

Figure 7.5: Auto spectra at (blue) CMI 2 and (red) CMI 4 for four time series (CMIe2, CMIe3, CMIe4, CMIe5). This figure shows that at the observed peak frequency, the energy at CMI 2 is always greater than at CMI 4.

CHAPTER 8: DISCUSSION

The observations of infragravity wave events on the reef flat are consistent with the excitation of a quarter-wavelength normal mode (Chapter 6). This normal mode infragravity frequency and period depends on the water level and the reef length according to Equation 6.10. Section 7.2 and Table 7.1 show that the observed peak frequency depends on the water level on the reef flat. Observations show that the peak frequency increases as the water level increases over the reef flat.

Observations on two reefs of different lengths allowed us to test the theoretical dependance of peak frequency on reef length. Section 7.3 and Table 7.2 shows the dependance of the peak frequency due to the reef length. Comparing observations of peak period from the ROI and CMI reefs, which have approximately 100 m difference in length, shows that when the reef length is shorter, the peak frequency is larger, consistent with the theoretical peak frequency Equation 6.10.

By comparing infragravity energy at the mid reef sensor and near shore sensor at ROI and CMI, we found that the energy near the peak frequency increased shoreward consistent with the excitation of a quarter-wavelength normal mode.

The modal excitation on the reef flat observed at ROI and CMI are consistent with the studies of *Nakaza et al.* (1990) and *Péquignet et al.* (2009). The first modal period is given by $T_0 = 4L/\sqrt{gh}$. This equation shows that when the period is proportional to the reef length, the period is also inversely proportional to the square root water level. These were dependancies observed both at ROI and CMI.

For this research, we have omitted dissipation from Equation 6.1. Dissipation includes the effects of friction over the reef flat. Dissipation may be important on reefs with longer cross shore length, and also for shallow water depths over the reef flat, and is the topic of further study.

An open question is how is the energy at the fore reef excites the normal modes on the reef flat. Preliminarily, there have been studies that suggest that the forcing connected to the infragravity energy is related to the envelope of the waves at the fore reef (*Nakaza et al.*, 1990; *Nakaza and Hino*, 1991; *Gourlay*, 1996; *Péquignet et al.*, 2009; *Nwogu and Demirbilek*, 2010; *Van Dongeren et al.*, 2013). *Nakaza et al.* (1990) and *Péquignet et al.* (2009) related the forcing of the infragravity waves on the reef flat to the wave envelope. The envelope of the wave is energetic at frequencies similar to the normal modes (Figure 8.1).

A potential issue that may arise in the future is if the reef flat water level rises due to sea level increases. It is well documented that large parts of the western pacific are experiencing sea level rise (e.g., *Merrifield and Maltrud*, 2011; *Perrette et al.*, 2013). This research demonstrated that the increase in water level will decrease the period of a normal mode. On the fringing reefs that *Péquignet et al.* (2009) and *Pomeroy et al.* (2012) studied, they did not see modal excitation of infragravity waves over the reef flat during normal conditions or at all. Sea level rise has the potential to increase the water level over these shallow and long fringing reefs, which may facilitate the excitation of similar to what was seen during Man-Yi at the Ipan reef (*Péquignet et al.*, 2009).

Under elevated water levels, the potential for normal modes to be excited may increase. The findings from this research suggests that the infragravity waves are and may become

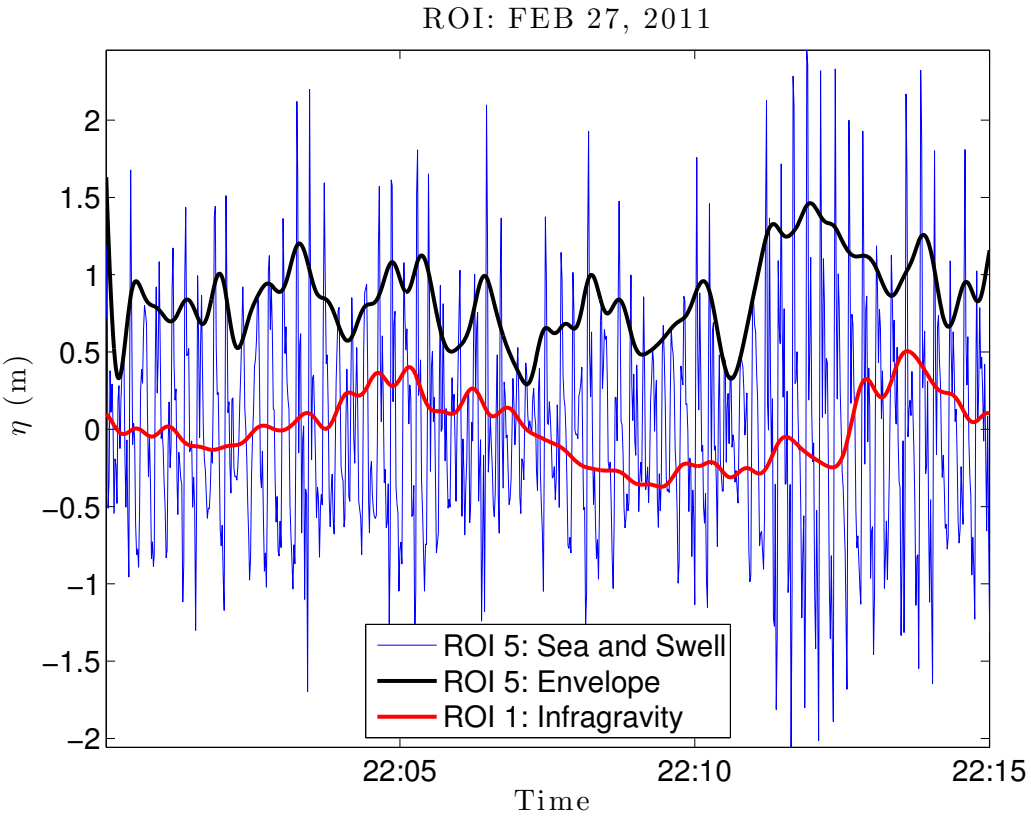

Figure 8.1: Free surface elevation of (blue) sea and swell component of the wave at ROI 5, the (black) envelope of the sea and swell component at ROI 5 and (red) the infragravity wave at ROI 1. This figure shows that the time scale of the envelope at ROI 5 and the infragravity wave at ROI 1 are similar.

an increasingly more important component in wave driven inundation. Low lying areas are already affected by sea level rise, just for the simple reason of the level of the land is close to sea level. This research suggests that the risk of wave driven inundation also may increase as sea level rise continues. Areas such as the Ipan reef under elevated water levels may experience modal excitation on the reef as commonly as the Republic of the Marshall Islands. These hypotheses are made under the assumption that the coral growth will be limited and will not grow fast enough to maintain the current water level over the reef flat. The forcing of these normal modes should be clarified to understand the infragravity waves further in order to evaluate the risk and vulnerability of the low lying areas world wide.

APPENDIX A: BAND WIDTH

The sensitivity of the frequency limits of the band pass filter is considered here. The appropriate frequency band of the infragravity and sea and swell depends on the spectral content of the observations. This also means that the frequency limits of the bands are not universal. Tests were conducted with different boundaries of the band pass filter. Table A.1 shows how the width of the band pass filter were arranged.

	All (Hz)	Infragravity (Hz)	Sea and swell (Hz)
Original	$1/900 < f < 0.35$	$1/900 < f \leq 1/30$	$1/30 < f < 0.35$
$IG_{1/25}$	$1/900 < f < 0.35$	$1/900 < f \leq 1/25$	$1/25 < f < 0.35$
$IG_{1/20}$	$1/900 < f < 0.35$	$1/900 < f \leq 1/20$	$1/20 < f < 0.35$

Table A.1: Data on the band width of the band pass filters used in this study.

The total band width has not been changed; however, the infragravity and sea and swell band widths have been varied to determine their effects on significant wave height. The assumption is that there will be more energy in the infragravity band, since more frequencies have been added. Figure A.1 shows the difference in significant wave height due to the change in the size of the band pass.

The figures makes it clear that the difference the width of the band pass filter is negligible for this data set. There are some visible peaks seen in Figure A.1, however, the percentage difference in the estimated significant wave height is negligible.

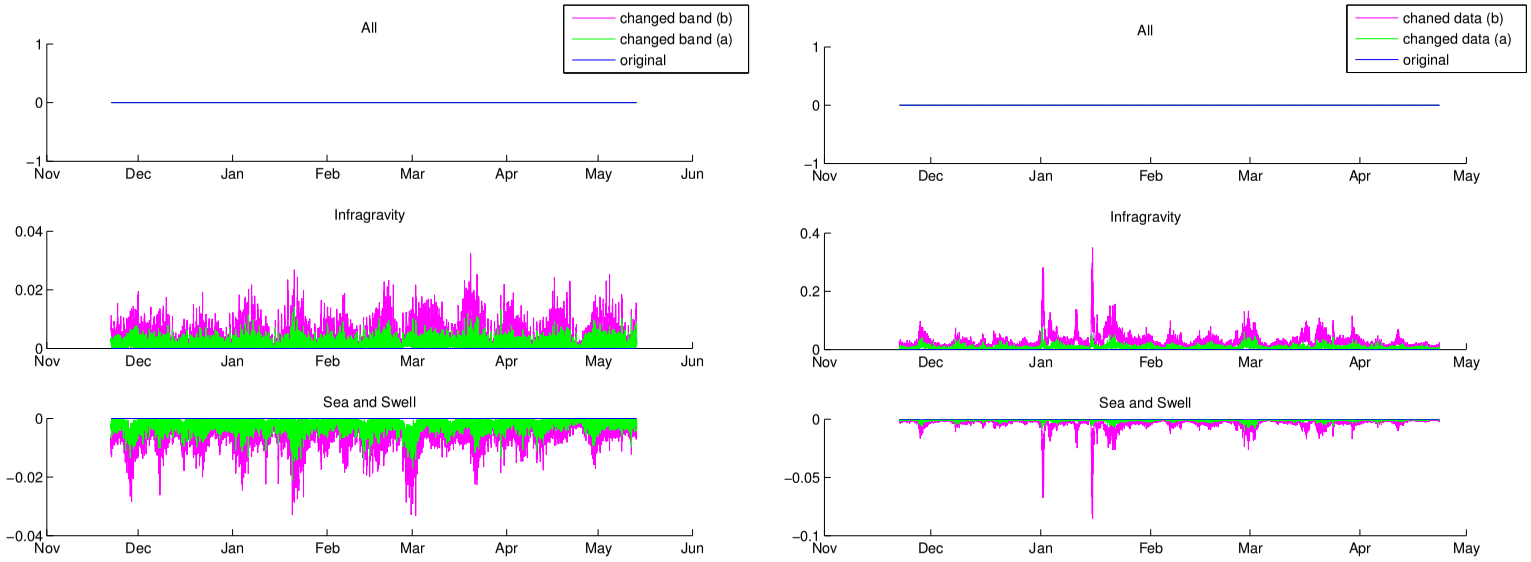

(a) ROI 1

(b) ROI 5

Figure A.1: The differences of the band width are examined with the significant wave height.

APPENDIX B: PEAK PERIOD ERRORS

Theoretically, the peak period on the fringing reef is estimated from the quarter-wavelength normal mode, formula $T_0 = 4L/\sqrt{gh}$. When the theoretical period is calculated, the reef length and the water level are the only two variables that affect the peak frequency. Therefore the inaccuracy of the reef length will contribute to an error in estimating the theoretical peak period.

Also, another error that may affect the theoretical peak period is the estimated water level. For the time series analyzed here, the water level is gradually increasing or decreasing due to the tidal effect. The water level is estimated by averaging the water depth during the chosen time series at the two sensors on the reef flat. Therefore, when the time series shows a tidally dependent water level, using a constant water level in the theoretical peak period is questionable.

The theoretical period for the events selected for investigation shown in Figure 5.2a and 5.3a is compared with the observed peak period at ROI and CMI in Tables B.1 and B.2. Due to the record length of the data, the frequency resolution at low frequency is limited. Given the uncertainty of the water depth, the inaccuracy of the reef length and resolution of the observed peak frequency, we find reasonable agreement between theoretical and peak periods in Table B.1 and B.2.

Record No.	Date	Water Level (m)	Observed Peak Frequency ($\times 10^{-3}$ Hz)	Observed Peak Period (sec)	Theoretical Peak Period (sec)
4697	FEB 27, 2011	0.64	1.76	568	480
1147	DEC 16, 2010	0.82	2.31	432	423
2635	JAN 16, 2011	0.84	3.06	372	417
769	DEC 08, 2011	0.93	2.50	400	397
302	NOV 28, 2010	1.0	2.50	400	383
2065	JAN 04, 2011	1.2	2.69	372	356
2886	JAN 21, 2011	1.2	3.06	327	350

Table B.1: Observed period versus theoretical period at ROI. By comparing the observed and theoretical peak period, the periods show better agreement when the water levels are higher.

Record No.	Date	Water Level (m)	Observed Peak Frequency ($\times 10^{-3}$ Hz)	Observed Peak Period (sec)	Theoretical Peak Period (sec)
5116	MAR 08, 2011	0.84	2.31	432	279
259	NOV 27, 2010	0.91	2.31	432	268
731	DEC 07, 2010	1.0	3.61	277	260
1875	DEC 31, 2010	1.2	3.80	263	219
3391	JAN 31, 2011	1.2	3.06	327	227

Table B.2: Observed period versus theoretical period at CMI.

REFERENCES

Dean, R. G., and R. A. Dalrymple (1991), *Water wave mechanics for engineers and scientists*, *Advanced Series on Ocean Engineering*, vol. 2, World Scientific Publishing Co Inc.

Ford, M., J. M. Becker, and M. A. Merrifield (n.d.), Case studies of atoll island inundation, Majuro Atoll, Republic of the Marshall Islands, *Unpublished Draft*.

Gourlay, M. R. (1996), Wave set-up on coral reefs. 2. Set-up on reefs with various profiles, *Coastal Engineering*, pp. 17–55.

Lugo-Fernandez, A., H. H. Roberts, and W. J. Wiseman, Jr (1998), Water level and currents of tidal and infragravity periods at Tague Reef, St. Croix (USVI), *Coral Reefs*.

Merrifield, M. A., and M. E. Maltrud (2011), Regional sea level trends due to a Pacific trade wind intensification, *Geophysical Research Letters*, *38*, doi:10.1029/2011GL049576.

Nakaza, E., and M. Hino (1991), Bore-like surf beat in a reef zone caused by wave groups of incident short period waves, *Fluid Dynamics Research*, *7*(2), 89–100, doi:10.1016/0169-5983(91)90062-N.

Nakaza, E., S. Tsukayama, and M. Hino (1990), Bore-like surf beat on reef coasts, *Coastal Engineering*.

Nwogu, O., and Z. Demirbilek (2010), Infragravity wave motions and runup over shallow fringing reefs, *Journal of Waterway, Port, Coastal, and Ocean Engineering*.

Péquignet, A. C., J. M. Becker, M. A. Merrifield, and S. J. Boc (2011), The dissipation of wind wave energy across a fringing reef at Ipan, Guam, *Coral Reefs*, *30*(S1), 71–82, doi:10.1007/s00338-011-0719-5.

Péquignet, A. C. N., J. M. Becker, M. A. Merrifield, and J. Aucan (2009), Forcing of resonant modes on a fringing reef during tropical storm Man-Yi, *Geophysical Research Letters*, *36*(3), doi:10.1029/2008GL036259.

Perrette, M., F. Landerer, R. Riva, K. Frieler, and M. Meinshausen (2013), A scaling approach to project regional sea level rise and its uncertainties, *Earth System Dynamics*, *4*(1), 11–29, doi:10.5194/esd-4-11-2013.

Pinet, P. R. (2009), *Essential invitation to oceanography*, Burlington, MA : Jones & Bartlett Learning.

Pomeroy, A., R. Lowe, G. Symonds, C. Moore, and A. van Dongeren (2012), The dynamics of infragravity wave transformation over a fringing reef, *Journal of Geophysical Research*, *117*(C11), doi:10.1029/2012JC008310.

Spennemann, D. H. R. (1998), Non-traditional settlement patterns and typhoon hazard on contemporary Majuro Atoll, Republic of the Marshall Islands.

Van Dongeren, A., R. Lowe, A. Pomeroy, D. M. Trang, D. Roelvink, G. Symonds, and R. Ranasinghe (2013), Numerical modeling of low-frequency wave dynamics over a fringing coral reef, *Coastal Engineering*, *73*, 178–190.

Vetter, O., J. M. Becker, M. A. Merrifield, A. C. Péquignet, J. Aucan, S. J. Boc, and C. E. Pollock (2010), Wave setup over a Pacific Island fringing reef, *Journal of Geophysical Research*, *115*(C12), doi:10.1029/2010JC006455.